

CONTENTS

Proceedings of the 16th NICT TDC Symposium (Kashima, June 21, 2017)

| | |
|---|----------|
| A numerical study on a photonic assisted analog-to-digital converter operating at 100 GSa/s | 1 |
| <i>K. Furusawa, I. Morohashi, N. Sekine and I. Hosako</i> | |
| Water Vapor Radiometer for Radio Astronomy and Volcano Monitoring | 5 |
| <i>Noriyuki Kawaguchi</i> | |
| Radio Frequency Interference in GNSS Observations by Artificial Signals for Mobile Phones | 10 |
| <i>Yoshihiro Fukuzaki, Tomokazu Nakakuki, Yuji Miura, Asuka Sato, Hiromichi Tsuji</i> | |
| Look back on 18 years of Tsukuba 32-m antenna | 14 |
| <i>Midori Fujiwara, Shinobu Kurihara, Masayoshi Ishimoto, Takahiro Wakasugi, Michiko Umei</i> | |
| Phase-up twin antennas for high-sensitivity maser observations | 17 |
| <i>Kazuhiro Takefuji, Koichiro. Sugiyama, Yoshinori Yonekura, Tagiru Saito, Kenta Fujisawa, and Tetsuro Kondo</i> | |
| Development of Wideband Antenna | 21 |
| <i>Hideki Ujihara</i> | |
| 'Node - HUB' Style VLBI with Broadband System. | 22 |
| <i>Mamoru Sekido</i> | |

Technical Reports

| | |
|--|----------|
| Holographic Measurement for Kashima 34 meter Antenna | 26 |
| <i>Kazuhiro Takefuji, Masanori Tsutsumi, Eiji Kawai, and Mamoru Sekido</i> | |
| Recent progress of K5 software correlation system | 29 |
| <i>Tetsuro Kondo</i> | |

A numerical study on a photonic assisted analog-to-digital converter operating at 100 GSa/s

K. Furusawa (*kfurusawa@nict.go.jp*),
I. Morohashi, N. Sekine and I. Hosako,

Frontier Research Laboratory,
National Institute of Information and
Communications Technology (NICT),
4-2-1, Nukuikitamachi, Koganei, Tokyo, Japan

Abstract: The feasibility of a photonic-assisted analog-to-digital converter (p-ADC) based on a frequency comb source operating at 10 GHz in the telecommunication C band is numerically investigated. It is found that the effective number of bits (ENOB) monotonically decreases with the input RF frequencies. Nevertheless, $\text{ENOB} > 4$ can still be anticipated at the Nyquist sampling rate of 50 GHz using only 10 WDM channels by managing the temporal allocation of spectral channels.

1. Introduction

Analog-to-digital converters are ubiquitously used at the frontends in varieties of signal processing systems. The performance measures are typically characterized by sampling rates and effective noise of bits (ENOB). Despite constant progress of digital electronics speeds, the progress in ultrafast ADCs (> 10 GHz) used for dedicated applications such as optical / ultrawideband wireless communications and data acquisitions in astronomy and geodesy are rather slow; typically 1.5 bits per 8 years, as reported by Walden[1]. One of the major reasons is an aperture jitter of temporal sampling. In general, ENOB degrades 4 bits / octave for a given amount jitter. At present, a clock jitter is about 100 fs for laboratory instruments. This implies that the achievable ENOB is less than 3 at 100 GHz. Then, it is evident that the improvement in timing jitter is the key issue for analog signal sampling beyond 100 GHz. In addition, finite transit time of the transistors used in the comparators leads to so-called comparator ambiguities, which impose a more serious impediment for high speed sampling in electronic ADCs (typically beyond 10 GHz). On the other hand, extremely low timing jitter has already been achieved in mode-locked solid-state lasers, owing to very short temporal duration of optical pulses and a high intracavity pulse energy[2]. This fact has motivated a renewed interest in photonic assisted form of ADCs for high speed applications.

Photonic ADCs (p-ADC) have rather a long history since 1970's and various architectures have so far been proposed. An excellent review was given by Valley[3]. Recent successful developments in p-ADCs include use of the time-stretch principle[4], pioneered by Jalari *et al.*, with which the sampling rate beyond 1 TSa/s has been reported[5]. In view of integrating the entire system on a silicon photonics chip, Kärtner *et al.* demonstrated 7 ENOB for a 40 GHz signal[6], employing off-the-shelf components as a preliminary result, where the discrete time-frequency mapping scheme was used in conjunction with narrowband detection. These studies have clearly demonstrated the potential of p-ADCs in scaling the sampling speeds. On the other hand, there are a number of issues such as sensitivity and realtimeliness. The latter is particularly relevant to telecom applications since the signal captured by the ADC should eventually be regenerated from the DAC output. In addition, the perfect reconstruction condition is not warranted for this type of ADCs due partly to the complexity of the photonic analog link, which may call for new types of equalization schemes.

In this study, we specifically consider utilization of a frequency comb generator (FCG)[7] operating at 10 GHz in a system based on the discrete time-frequency mapping scheme (see Fig.1). By employing a high repetition rate light source, the number of optical components in the ADC system can be reduced, thereby greatly simplifying the system architecture. Furthermore, since the external RF clock source determines the timing jitter performance of the FCG, the timing jitter issues in p-ADCs can be diverted to the accuracy of the clock: as we improve the clock performance, the jitter performance of the system can also be improved without modifying the entire system. However, our preliminary study has shown that this type of system is spectrally hungry due to the cross talks in both temporal and spectral domains. It becomes increasingly difficult to retain a low level

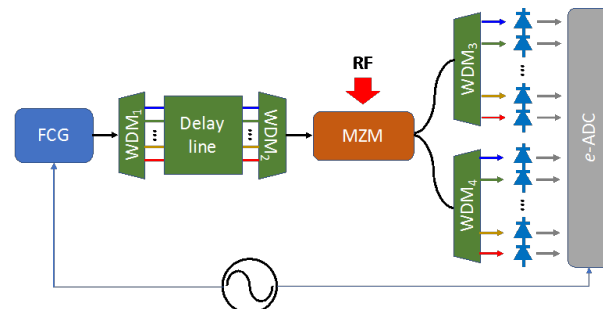


Figure 1. Schematic of p-ADC system based on discrete time-frequency mapping scheme.

of timing jitter as the spectral bandwidth is increased since additional nonlinear spectral broadening may seriously deteriorate the original jitter performance[8]. In order to make a system more spectrally efficient, we propose a frequency hopping (FH) approach similarly to optical code-division multiplexing systems[9]. By using appropriate allocation of the spectral channels in time domain, the cross talks originated from the adjacent spectral channels can be reduced significantly. We discuss the design criteria of the proposed system and numerically show how the spectral bandwidth requirement can be relaxed in a system operating at 100 GSa/s.

2. Description of the system

We assume a FCG operating at 10 GHz repetition rate, for which timing jitter as low as 11 fs has been reported[10]. This suggests potentially achievable ENOB of 7 for an input frequency of 50 GHz. We assume a number of spectral channels $N = 10$ so as to accomplish the sampling rate of 100 GSa/s. The FCG output was spectrally sliced by an arrayed waveguide grating (AWG) followed by the delay lines, with which each spectral channel is assigned to a specific timing within the repetition interval. After combining all channels using another AWG, the RF signal is optically-sampled using a Mach-Zehnder electro-optic modulator (MZM)[11] with two complementary output ports. These outputs are spectrally separated by the AWGs again and each channel is individually detected by the photodiodes. Then, the electrically converted signals are quantized by electronic ADCs (e-ADCs). This system allows us to scale the sampling speed by a factor of N while maintaining the bandwidth requirement for the e-ADCs to the repetition frequency of the FCG. Detection of two complementary outputs allows for linearization of MZM[12]. The details of the model are described in Ref. [13]. The transmission profiles of the spectral channels through the AWGs were assumed to be hyper-gaussian.

3. Frequency-hopping (FH) scheme

In designing the above p-ADC system, each spectral channel has to be wide enough to avoid sampling the adjacent time slots (temporal cross talks). Similarly, flat phase responses of the channels are also important to generate a train of nearly Fourier-transform limited pulses since any pedestals due to the residual chirp penetrating to the adjacent time slots results in temporal cross talks. On the other hand, spectral cross talks should also be minimized for signal detection. From these simple arguments, the total bandwidth required for the light source

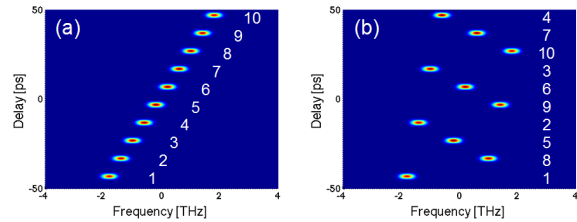


Figure 2. Time-frequency representation of a sampling pulse train in (a) linear and (b) FH assignment, generated by taking cross correlations with a transform-limited gaussian pulse with 500 GHz bandwidth (i.e. crosscorrelation frequency resolved optical gating (XFROG) trace[14]).

(Δf_{source}) can be estimated to $9.2N/T_S$, where T_S is the sampling period, assuming the gaussian profiles of the spectral channels. This suggests that the source bandwidth spanning from C to L bands (wavelength of $1.53 \sim 1.61 \mu\text{m}$) is required to achieve the sampling rate of 100 GSa/s ($T_S = 10$ ps). To relax this bandwidth requirement, we consider an allocation method of the spectral channels in time domain. We label spectral channel numbers (1 ~ 10) from the low frequency side. If we solely assign them in order in the time domain (linear assignment: see Fig.2 (a)), the spectral cross talks should also appear in the neighboring time slots in the detected signals at the photodiodes. Then, the natural strategy would be to separate the temporal distance of adjacent spectral channels as much as possible. For instance, in the case of $N = 10$, the minimum channel separation ΔN can be set to 3 (frequency hopping (FH) assignment: e.g. [1 8 5 2 9 6 3 10 7 4], see Fig.2(b)). Then, it becomes possible to eliminate the spectral cross talks by temporal gating (with the gating duration of $\sim T_S \Delta N$), which can be implemented using slightly faster e-ADCs (with their sampling rates of $1/(T_S \Delta N)$). Note that this approach can be even more effective in a system consisting of many channels with a low repetition rate light source since ΔN can be increased by increasing N although the total bandwidth required for the source is increased (since the channel width should be retained to avoid temporal cross talks).

4. Numerical example

To verify the effectiveness of the FH scheme, we calculated the ENOB as a function of input RF frequency. The errors in p-ADC output signals depend on the input frequency as well as the phase. By average the phase dependence, nominal ADC errors $\Delta \nu$ were first calculated, for which intrinsic signal-to-noise ratio (SNR) is defined. Then, the

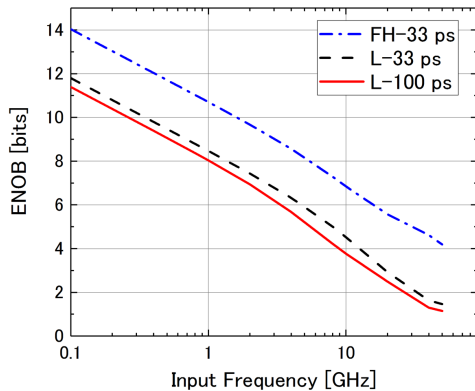


Figure 3. ENOB as a function of input RF frequency for linear (L) and frequency hopping (FH) assignment with different integration time.

ENOB was calculated by the standard formula[3]:

$$ENOB = \frac{SNR - 1.76}{6.02} \quad (1)$$

In AWGs, hyper-gaussian channels with their bandwidths of 400 GHz and a uniform side mode suppression ratio (SMSR) of 30 dB were assumed. The channel spacing was also set to 400 GHz. Then, the total bandwidth of the source amounts to 4 THz that can be covered in the telecommunication C band. Residual phases were neglected. Three cases were studied: 1) 100 ps and 2) 33 ps integration time with linear assignment, and 3) 33 ps integration time with FH assignment. The results are compared in Figure 3. In all cases, ENOB monotonically decreases with the RF frequency due to the temporal cross talks since the amplitude difference between the adjacent time slots increasingly becomes large for high frequency inputs. For the case 1), additional spectral cross talks further degrade the ENOB performance, consequently resulting in the ENOB less than 2 at the Nyquist frequency of 50 GHz. Even when the integration time is shortened to 33 ps (case 2)), the improvement in ENOB is subtle since the elimination of the spectral cross talks is not effective due to the linear spectral allocation. By contrast, the ENOB can drastically be improved by using the FH assignment (case 3)), as anticipated, resulting in the ENOB of > 4.3 at 50 GHz. Note that a broadband FCG spanning over 4 THz has already been realized in the experiment[15]. Therefore, it seems feasible to achieve such p-ADC performance, provided that its timing jitter is sufficiently low (< 80 fs).

5. Summary

We have numerically investigated the performance of a p-ADC system operating at 100 GSa/s based on discrete time-frequency mapping scheme using a 10 GHz frequency comb generator light source. Assuming a realistic amount of cross talks, it is shown that the ENOB degrades with an increase in input RF frequency (~ 3.4 bits / octave). Furthermore, it is also demonstrated that appropriate assignment of the spectral channels in time domain is useful for relieving the bandwidth requirement with the aid of fast e-ADCs. As a result, it is anticipated that $ENOB > 4$ can be obtained at the Nyquist frequency of 50 GHz.

Acknowledgement

K.F. wishes to acknowledge Drs. A. Kanno, Y. Yoshida, and T. Sakamoto (Network systems laboratory, NICT) for fruitful discussions.

References

- [1] Walden, R. H., "Analog-to-digital converter survey and analysis", IEEE Journal on selected areas in communications, Vol. 17, No. 4, pp. 539-550, 1999.
- [2] Haus, H. A., and Mecozzi, A., "Noise of mode-locked lasers", IEEE Journal of Quantum Electronics, Vol. 29, No. 3, pp. 983-996, 1993.
- [3] Valley, G. C., "Photonic analog-to-digital converters", Optics Express, Vol. 15, No. 5, pp. 1955-1982, 2007.
- [4] Mahjoubfar, A., Churkin, D. V., Barland, S., Broderick, N., Turitsyn, S. K., and Jalali, B., "Time stretch and its applications", Nature Photonics, Vol. 11, No. 6, pp. 341-351, 2017.
- [5] Chou, J., Boyraz, O., Solli, D., and Jalali, B., "Femtosecond real-time single-shot digitizer", Applied Physics Letters, Vol. 91, No. 16, p. 161105, 2007.
- [6] Kim, J., Park, M. J., Perrott, M. H., and Kärtner, F. X., "Photonic subsampling analog-to-digital conversion of microwave signals at 40-GHz with higher than 7-ENOB resolution", Optics Express, Vol. 16, No. 21, pp. 16509-16515, 2008.
- [7] Sakamoto, T., Kawanishi, T., and Izutsu, M., "Widely wavelength-tunable ultra-flat frequency comb generation using conventional dual-drive Mach-Zehnder modulator", Electronics Letters, Vol. 43, No. 19, pp. 1039-1040, 2007.

- [8] Ishizawa, A., Nishikawa, T., Mizutori, A., Takara, H., Takada, A., Sogawa, T., and Koga, M., "Phase-noise characteristics of a 25-GHz-spaced optical frequency comb based on a phase- and intensity-modulated laser", *Optics Express*, Vol. 21, No. 24, pp.29186-29194, 2013.
- [9] Fathallah, H., Rusch, L. A. and LaRochelle, S., "Passive optical fast frequency-hop CDMA communications system", *Journal of Lightwave Technology*, Vol. 17, No. 3, pp.397-405, 1999.
- [10] Metcalf, A. J., Quinlan, F., Fortier, T. M., Diddams, S. A., and Weiner, A. M., "Broadly tunable, low timing jitter, high repetition rate optoelectronic comb generator", *Electronics letters*, Vol 51, No. 20, pp. 1596-1598, 2015.
- [11] Taylor, H. F., Taylor, M. J. and Bauer P. W., "Electro-optic analog-to-digital conversion using channel waveguide modulators", *Appl. Phys. Lett.* Vol. 32, No. 9, pp. 559-561, 1978
- [12] Seifler, G. A., Chou, J., Conway, J. A., and Valley, G. C., "Distortion correction in a high-resolution time-stretch ADC scalable to continuous time", *Journal of Lightwave Technology*, Vol. 28, No. 10, pp. 1468-1476, 2010.
- [13] Khilo, A., "Integrated optical analog-to-digital converter" (Doctoral dissertation, Massachusetts Institute of Technology) 2008.
- [14] Trebino, R., "Frequency-resolved optical gating: the measurement of ultrashort laser pulses", Springer Science Business Media, 2012.
- [15] Morohashi, I., Sakamoto, T., Sotobayashi, H., Kawanishi, T., Hosako, I., and Tsuchiya, M., "Widely repetition-tunable 200 fs pulse source using a Mach-Zehnder-modulator-based flat comb generator and dispersion-flattened dispersion-decreasing fiber", *Optics letters*, Vol. 33, No. 11, pp.1192-1194, 2008.
-

Water Vapor Radiometer for Radio Astronomy and Volcano Monitoring

Noriyuki Kawaguchi (*kawagu.nori@nao.ac.jp*),

National Astronomical Observatory of Japan,
2-21-1 Osawa, Mitaka Tokyo, Japan

Abstract: A water vapor radiometer has been used for monitoring delay and absorption caused on a radio wave travelling through the troposphere, primarily caused by water vapor and liquid water. The measured data is used as delay calibration on geodetic VLBI observations and source brightness calibration on radio astronomy observations. The water vapor in a volcano fume also shall be measured to monitor the volcano activity, which is crucially important in Japan of volcanic islands where many volcanos are located in active, and some are erupting.

In this paper the importance of water vapor monitoring in radio astronomy, geodetic VLBI measurements and monitorings of volcano activities.

1. Introduction

NAOJ, National Astronomical Observatory of Japan has started the development of a water vapor radiometer (WVR) for precise radio astronomy of VERA (Kawaguchi 2016) [1]. The development aims at obtaining precise delay correction for VERA observations to get better geodetic and astrometric solutions. The radiometer is also expected to be used in flux calibration for a radio astronomy observation to measure the true brightness of a target source.

The radiometer is designed to measure total column density of water vapor toward the sky covered by a single beam of the WVR antenna. The air in the beam contains not only water vapor but also liquid water, Oxygen, Nitrogen and minor constituents. The Oxygen and Nitrogen (Dry Component) is uniformly distributed in the atmosphere and is easy to predict the delay and absorption by monitoring the slowly changing ground pressure measured by a ground weather station. The water vapor and liquid water (Wet Component) are heavily localized in the atmosphere. The delay and the absorption is rapidly changing in time. The humidity measurements on a ground is helpless to measure a total amount of the wet components in the atmosphere. A rain meter provides us good information if the liquid water drops down on the ground at a time of raining. The rain causes heavy attenuation and makes system noise temperature

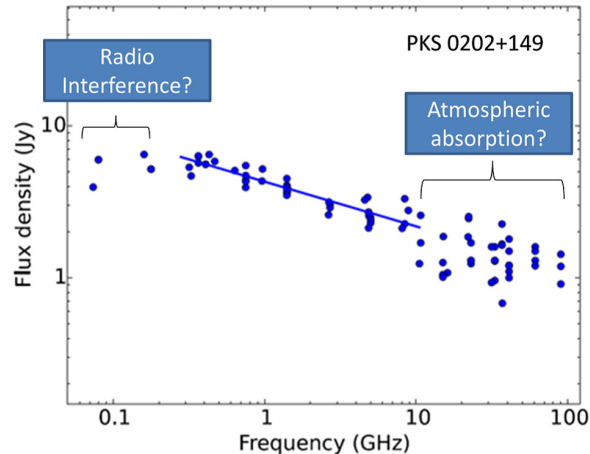


Figure 1. Radio spectrum of PKS0202+129

of a radio astronomy telescope unacceptably high. The liquid water content in a cloud is impossible to measure without a water vapor radiometer. These bad impacts will be discussed in the next section. The water vapor content in a volcano fume is important to understand the state of the volcano activity and to predict the eruption. So far the water content in the fume has been indirectly estimated by measuring SO_2 or other constituents with an optical laser. In the measurement the mixing ratio of H_2O/SO_2 is assumed as is empirically known (Burton 2000)[2] (Writter 2012)[3]. Direct measurement of water vapor in the volcanic fume will be discussed in chapter 3. In chapter 4 the importance of a water vapor radiometer will be noted.

2. Impacts on Radio Astronomy and VLBI Geodesy

Fig.1 shows the radio flux spectrum of PKS0202+129 referenced to the the NASA/IPAC Extragalactic Database (NED). As clearly seen on the figure, flux densities above 10GHz is largely scattered, probably caused by large uncertainty in the atmospheric absorption. The absorption changes day by day depending on the weather condition on the day, water vapor and liquid water content in the air. If a dark cloud passes over the radio telescope, a large fluctuation on the brightness of a target source may happen in a short time scale. It is uncorrectable, even if we observe a well-calibrated source as a flux standard.

It varies with time as is shown in Fig.2 (Forkman 2003)[4]. Radio astronomers recently pay great attention on the intra day variable sources of AGN(IDV) [5]. They need to observe the sources under a clear sky of stable atmosphere or to make careful correction on the atmospheric absorption, otherwise they may misjudge the variability with

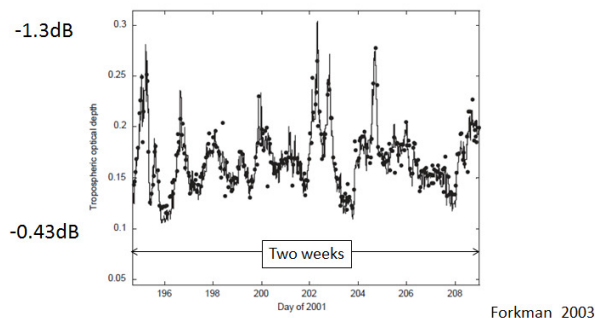


Figure 2. Radio spectrum of PKS0202+129

fluctuations of the atmospheric absorption.

Geodeticist nowadays succeeds in positioning a VLBI station in a few millimeters on a local horizontal plane (Jike 2017)^[6]. Fig.3 shows the 3D formal error diagram. The vertical error is almost six times larger than the horizontal error. In theory, the vertical error is twice the horizontal error. The excess in the vertical error might be caused by the uncertainty in EPL, Excess Path Length, of the atmospheric propagation path. The major error source is the water vapor in the atmosphere. Liquid water does not cause the delay on radio wave propagation.

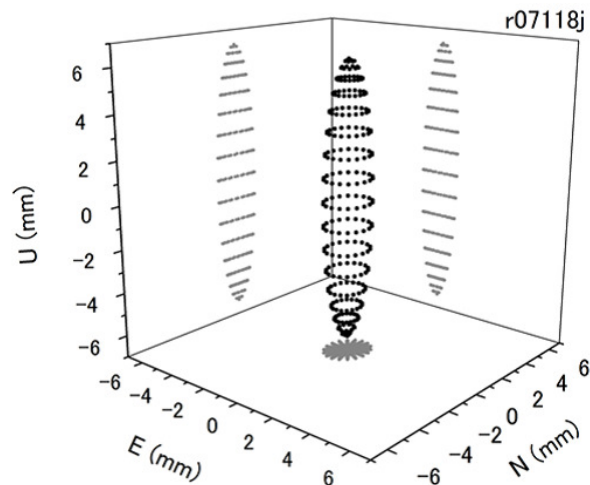


Figure 3. Geodetic VLBI measurement error

Like as Geodeticists, the influence of water vapor in the atmosphere is also a serious problem for radio astronomical observers working on precise astrometry. Fig.4 shows annual parallax measured on G48.61+0.02 to study the galaxy rotation by VLBI in right ascension and declination (Nagayama 2011)^[7]. Equivalent path length strongly depends on a total amount of water vapor in the propagation path and an elevation angle. We can

see in Fig. 4 that astrometry errors in the declination are much larger than those in the right ascension. The position in declination is much more sensitive to the elevation angle and the water vapor content than that in the right ascension. Wa-

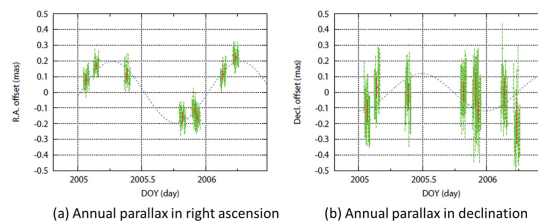


Figure 4. Large astrometry error in declination

ter vapor in the atmosphere shall be measured and corrected in geodesy and radio astronomy but has never been tried to use a WVR in Japanese observatories except the K3 WVR (Kawaguchi 2016)^[1]. The NAOJ has started the development of a new WVR in 2017 which will be briefly introduced in the section 4.

3. Volcano Monitoring

In 2014, Ontake, one of Japanese active volcanoes, suddenly exploded and many mountain climbers more than 50 were dead (See Fig.5). No abnormal phenomenon were perceived before the eruption.



Figure 5. Disaster in Ontake in 2014

Volcanologists pointed out a fact that water vapor content in the volcanic fume quickly decrease as shown in a table of Fig.6 (Burton 2007)^[8]. In my private opinion the decrease of the water vapor is a serious sign of eruption, indicating the orifice of gas discharging is closed and the internal pressure is going high and high. In other words, if we monitor a continuous leak of water vapor from a volcanic mountain, we can recognize the internal pressure does not reach at a dangerous level of the explosion.

| Gas features | Quiescent degassing | Typical explosion | Smaller explosions |
|--|---------------------|-------------------|--------------------|
| H ₂ O % | 82.9 | 64.4 | 79.3 |
| CO ₂ % | 13.6 | 33.1 | 19.0 |
| SO ₂ % | 1.7 | 1.8 | 1.15 |
| HCl % | 1.7 | 0.33 | 0.43 |
| CO % | 0.03 | 0.44 | 0.15 |
| COS % | b.d. | 0.008 | b.d. |
| H ₂ O/CO ₂ | 6.1 | 2.3 ± 0.8 | 4.5 ± 2.3 |
| CO ₂ /S | 7.8 | 20.7 ± 2.1 | 16.8 ± 1.9 |
| S/Cl | 1.0–1.5 | 4.7 ± 0.8 | 2.5 ± 0.8 |
| CO/SO ₂ (10 ⁻²) | 1.8 | 24.0 ± 0.9 | 14.6 ± 0.4 |
| CO/CO ₂ (10 ⁻²) | 0.21 | 1.14 ± 0.09 | 0.9 ± 0.08 |
| Equil. temp. (°C) | 700 | 1020–1130 | 1000–1060 |
| Source pressure (MPa) | ≤0.3–4 | ~70–80 | ~20–50 |

Figure 6. Decrease in the water vapor, is it a sign of eruption?

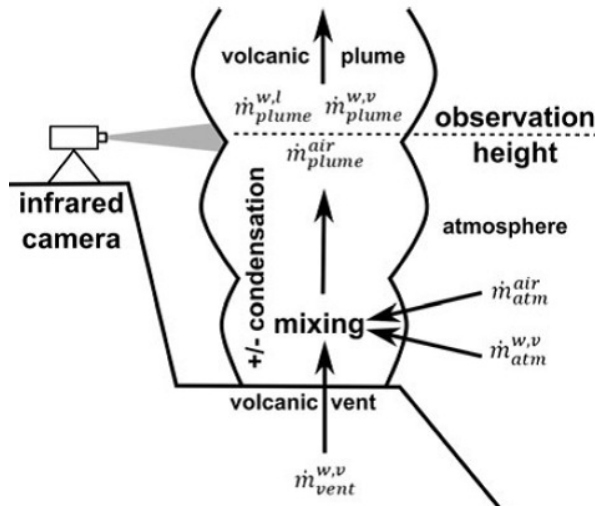


Figure 7. Indirect H₂O monitoring

The volcano monitoring for water vapor is important and was tried and presented by some authors (Witter 2012)^[9](Shinohara 2008)^[10]. The Witter shows an indirect way of measurements by using an infrared camera (See Fig.7) and the Shinohara suggests a mass ratio of H₂O against CO₂ and SO₂. They estimated a total content of water vapor by measuring CO₂ and SO₂ by using the mixing ratio estimated in advance.

Direct detection of water vapor was first tried by (Brian 2016)^[10] with a radiometer of frequencies of 22/183/232.5GHz. Excess brightness against the background emission observed in the volcanic fume at 22GHz is 1.5K as shown in Fig.8. The 183-GHz spectrum is inversely folded downward due to the extremely high sensitivity at the frequency, which is probably a good tracer for thin water vapor at high altitude or at a freezing cold place. The 232.5-GHz emission is too weak to measure the water vapor content in volcanic fumes. The water vapor emission at around 22GHz is probably the best. A new WVR was designed on the frequency range from 16GHz to 24GHz. A theoretical water vapor spectrum is shown in Fig.9, which indicates a total

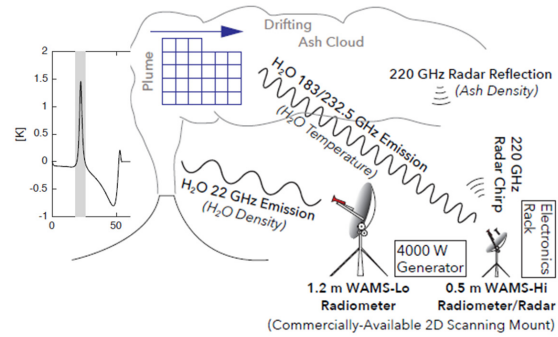


Figure 8. Trial of direct H₂O imaging

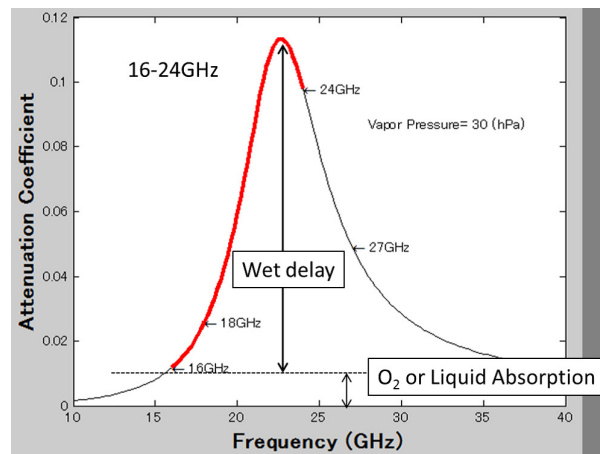


Figure 9. A H₂O emission spectrum around 22GHz at the water vapor content of 30hPa.

absorption through a line of sight. The peak from a base indicates the attenuation by the water vapor and the base is the attenuation caused by the Oxygen and the liquid water. The wideband spectrum makes possible to extract the water vapor content separated from the attenuation caused by the dry air and the liquid water. The attenuation spectrum is easily converted the emission spectrum by considering a height profile of temperature and by introducing a radiation transfer equation.

4. A compact and cost-effective WVR designed for a radio telescope

Commercial available WVRs are shown in Fig.10. The upper WVR is from Radio Physics co. ltd. in Germany and the lower from Radiometrics co. ltd. in USA. Both WVR are equipped with pointing drives on both azimuth and elevation axes, weather sensors and a GPS receiver. These ancillaries makes expensive in the cost. A radio telescope has already being equipped with these facilities so that a WVR on the radio telescope is possible to make as much more simple as possible.



Figure 10. Commercial available WVRs: the upper from Radio Physics and the lower from Radiometrics.

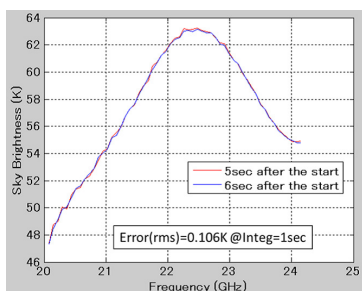


Figure 11. A wideband digital spectrometer on the KEK WVR

A new WVR developed by NAOJ consists of a feed horn, a simple receiver and a high speed digital spectrometer. In the first step the digital spectrometer was attached on the high-end receiver of the KEK, High Energy Accelerator Research Organization in Japan. The amplifier of the KEK receiver is a low noise amplifier cooled down below 50K and the frequency coverage is wide enough from 18GHz to 32GHz. The receiver noise temperature is 40K. The digital spectrum is measured at the time interval of one second. The one-second integrated spectrum at adjacent one-second samples is shown in Fig.11. The rms deviation between two one-second samples was 0.106K which corresponds to 0.45mm in EPL, Excess Path Length, and 0.07mm in PW, Precipitable Water. The precision is good enough

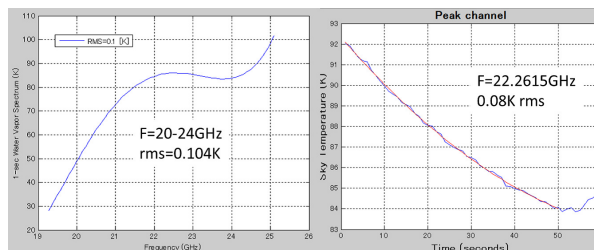


Figure 12. Frequency Spectrum and the time stability of a simplified WVR

and as good as commercial WVRs. The measurement error depends on the receiver noise and the bandwidth as an equation below,

$$Error(rms) = \frac{T_{sys}}{\sqrt{2B\tau}} \cdot \frac{\sqrt{2}}{q}, \quad (1)$$

where T_{sys} is a system noise temperature, a sum of a receiver noise temperature (40K in case of the KEK receiver) and a sky noise ($\sim 60K$), B is bandwidth (72.75MHz), and τ is an integration time (one second). All values in parenthesis are the best estimated value for the sky noise temperature and the setting parameters at a time of this experiment. The q is a digital quantization loss (0.85 here for 3-bit quantization). The theoretical expected error is 0.05K. The actual observed error is twice larger than the expected error, which shall be studied in the later work.

As we can see in the equation, even if the receiver noise increases from 40K to 180K in case that an amplifier is not cooled and exposed in the room temperature environment, the system noise temperature increases only by a factor of 2 for the sky noise temperature of 90K under humid weather. Thus a new compact WVR uses a room temperature amplifier to keep the cost reasonable. The new WVR was tested in a factory and the result is shown in Fig.12. The water vapor emission is shown in the spectrum (frequency profile) in left of the figure and the time profile of the spectrum peak at 22.26GHz in the right. The rms error is about 0.1K corresponding to the theoretically expected error. The simplified WVR will be mounted on the Mizusawa 20-m telescope in Japanese fiscal year of 2017.

5. Concluding Remarks

A water vapor radiometer, WVR, is useful to estimate the water vapor content in the atmosphere and to calibrate delay and absorption for geodetic/astronomical observations. A new compact WVR is now under development in Japan with financial support of NAOJ, which will be installed

in the Mizusawa 20m radio telescope in 2017 and expected to improve the astrometric accuracy better.

The WVR will be a powerful tool in predicting volcanic eruption if the single beam receiver would be assembled into a multi beam phased array. The array will be draw water vapor distribution over volcanoes. An imaging technique developed by radio astronomers will effectively applied to draw the map. The water vapor is invisible so that the ejection hole is hard to be specified (See Fig.13). Radio detection of water vapor emission makes possible to identify a place where explosion would happen in future. The sudden decrease of H_2O in a volcanic fume would be a serious sign of volcanic eruption, which might be useful to alert dangerous explosions.

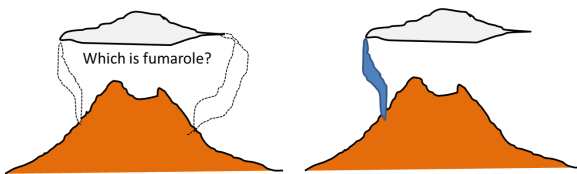


Figure 13. Which is a real fumarole position?

6. Acknowledgments

The author acknowledges to research collaborators, Dr. Yusuke Kohno and Dr. Tomoaki Oyama of NAOJ, National Astronomical Observatory of Japan, Dr. Taketo Nagasaki of KEK, High Energy Accelerator Research Organization, and Dr. Takashi Maeda of JAXA, Japan Aerospace Exploration Agency. A new water vapor radio meter is now being developed with them under a financial support of NAOJ. In the KEK experiment and the factory tests I received great helps of Mr. Kenichi Harada and Mr. Yuichi Chikahiro, engineers in Elecs co. ltd.. Here I would like to express my great thanks to them.

References

- [1] Kawaguchi, Water Vapor Radiometer: Challenge Again, Technology Development Center News, National Institute of Information and Communications Technology, Serial No. 36, page 4, November 2016
(http://www2.nict.go.jp/sts/stmg/ivstdc/news36/tdc_news36.pdf).
- [2] MBurton, M. R., Oppenheimer, C., Horrocks, L. A., Francis, P. W., Remote sensing of CO₂ and H₂O emission rates from Masaya volcano, Geology, vo. 28, No. 10, pp. 915-918, October 2000.
- [3] Witter, J. B., Hernandez, P., Harris, A. J. L. and Preéz, N., Quantification of the Mass Flux of H₂O Gas (Steam) at Three Active Volcanoes Using Thermal Infrared Imagery, Pure Appl. Geophys., vol. 169, pp. 1875-1889, 2012
- [4] Forkman, P., Erikssonb, P., Winnberg, A., The 22 GHz radio-aeronomy receiver at Onsala Space Observatory, Journal of Quantitative Spectroscopy & Radiative Transfer, vol. 77, pp. 23-42, 2003
- [5] Taeseok Lee, Sascha Trippe, Junghwan Oh, Do-Young Byun, Bong-Won Sohn, and Sang-Sung Lee, A SEARCH FOR AGN INTRADAY VARIABILITY WITH KVN, Journal of the Korean Astronomical Society, vol. 48, pp. 313-323, 2015
- [6] Adoption of K-band in the VERA Internal Geodetic VLBI and its Effectiveness, Jike, T., Manabe, S., Tamura, Y., Journal of the Geodetic Society of Japan, in printing, 2017.
- [7] Takumi Nagayama, Toshihiro Omodaka, Toshihiro Handa, Mareki Honma, Hideyuki Kobayashi, Noriyuki Kawaguchi, and Yuji Ueno1, Astrometry of Galactic Star-Forming Region G48.61+0.02 with VERA, Publ. Astron. Soc. Japan, vol. 63, pp. 719- 725, 2011
- [8] Mike Burton, Patrick Allard, Filippo Murée, Alessandro La Spina, Magmatic Gas Composition Reveals the Source Depth of Slug-Driven Strombolian Explosive Activity, SCIENCE, VOL. 317 No. 13, pp. 227-230, JULY 2007
- [9] J. B. WITTER, P. HERNANDEZ, A. J. L. HARRIS and N. PEÉREZ, Quantification of the Mass Flux of H₂O Gas (Steam) at Three Active Volcanoes Using Thermal Infrared Imagery, Pure Appl. Geophys. vol. 169, pp.1875-1889, 2012
- [10] H. Shinohara, A. Aiuppa, G. Giudice, S. Gurrieri, and M. Liuzzo, Variation of H₂O/CO₂ and CO₂/SO₂ ratios of volcanic gases discharged by continuous degassing of Mount Etna volcano, Italy, JOURNAL OF GEOPHYSICAL RESEARCH, VOL. 113, B09203, 2008
Space-Time Standards Group, NGNC, NICT, Kashima 34-m Radio Telescope 2007 Annual Report, 2008 (in Japanese).

Radio Frequency Interference in GNSS Observations by Artificial Signals for Mobile Phones

Yoshihiro Fukuzaki

(*fukuzaki-y96pe@milit.go.jp*),

Tomokazu Nakakuki, Yuji Miura, Asuka Sato, Hiromichi Tsuji

*Geospatial Information Authority of Japan,
1 Kitasato, Tsukuba Ibaraki, Japan*

Abstract: The Geospatial Information Authority of Japan installed Continuously Operating Reference Stations (CORSs) to receive GNSS signals in Japan and has maintained since 1996, and their number is more than 1,300 at present. The CORS network in Japan is now called GEONET (GNSS Earth Observation NETwork system). Recently radio communication using mobile phones (mobile telecommunications) is becoming more popular in Japan, and radio waves are transmitted in several frequency bands for the mobile telecommunications. One of the assigned frequency band is 1.475–1.511 GHz, which is located near the frequencies assigned for GNSS, L1 (1.57542 GHz) and L2 (1.2276 GHz). Since strong radio waves are transmitted from the radio towers for mobile telecommunications, Radio Frequency Interference (RFI) occurs at several GEONET stations with a specific receiver that are located near the radio tower and apparent height variations are detected.

We briefly report the apparent height variations of GEONET stations caused by RFI, discussion on its generation mechanism, and solution to solve this problem.

1. Introduction

The Global Navigation Satellite System (GNSS) including Global Positioning System (GPS) developed and maintained by the United States and Quasi-Zenith Satellite System (QZSS) by Japan is one of the space geodetic technologies. The Geospatial Information Authority of Japan (GSI) installed Continuously Operating Reference Stations (CORSs) to receive GNSS signals in Japan and has maintained since 1996, and their number is now more than 1,300. GSI's CORS network in Japan is now called GEONET (GNSS Earth Observation NETwork system). GEONET data are provided to public and private sectors and used for a lot of purposes in Japan, for example, public and private surveys, monitoring of crustal defor-

mations, location-based service, meteorology, ionosphere research, and so on.

Recently radio communication using mobile phones (mobile telecommunications) is becoming more popular in Japan, and radio waves are transmitted in several frequency bands for the mobile telecommunications. One of the assigned frequency band is 1.475–1.511 GHz, which is located near the frequencies assigned for GNSS, L1 (1.57542 GHz) and L2 (1.2276 GHz). Since strong radio waves are transmitted from the radio towers for mobile telecommunications, Radio Frequency Interference (RFI) occurs at several GEONET stations with a specific receiver that are located near the radio tower and apparent height variations are detected.

This paper gives the apparent height variations of GEONET stations caused by RFI, discussion on its generation mechanism and solution to solve this problem.

2. Apparent Height Variations

The time series of the height of 'Hakodate' that is one of the GEONET station are plotted in Figure 1. On May 27 in 2013 Signal-to-Noise ratios (SNR) of L1 and L2 signals became lower (L1: 45.1→42.7, L2: 31.9→30.2), and after this day obvious periodic variations were detected. Because no actual movement was detected by leveling measurement performed at the site, it is considered that the periodic variations are apparent. The similar height variations are also detected at several GEONET stations.

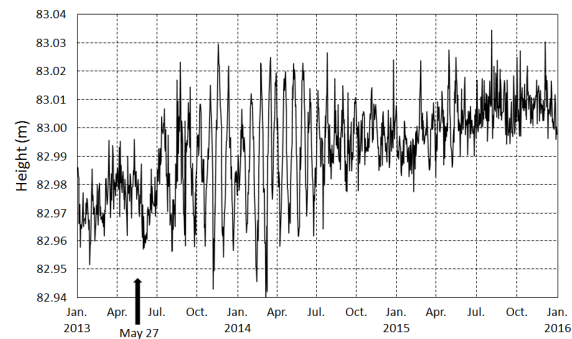


Figure 1. Time series of the height of the Hakodate station from Jan. 2013 to Dec. 2015.

At Hakodate, according to a mobile phone company, radio waves for the fourth generation of mobile telecommunications technology, which is called Long Term Evolution (LTE), started to be transmitted in those days before May 27, 2013. This suggests that the cause of the apparent variations is RFI by the strong radio waves for LTE. In the case of the other stations at which the similar vari-

ations are detected, there are also radio towers near the GEONET stations, so it is considered that the cause of the apparent height variation is the RFI by the strong radio waves for LTE.

It should be noted that a splitter that acted as the attenuator of -7 dB was inserted at the Hako-date station in September 2014 and replaced with the attenuator of -18 dB in October 2016.

3. Discussion on Generation Mechanism

The most serious influence of the strong RFI signals is saturation of amplifiers in the GNSS receiving system (GNSS antenna and receiver). Each amplifier has its own limit of the output level, and the amplifier saturation occurs when the strong radio wave whose level is over the amplifier limit is input. A conceptual figure of the amplifier saturation is shown in Figure 2. The input signals of the GNSS receiving system consist of a lot of wave components, and if the amplifier is saturated by the strong signal the saturated parts of all input waves are affected to be lack of their information and replaced with the highest values of their amplitude in both plus and minus sides. A schematic figure is shown in Figure 3. Because the frequencies of the LTE signal, L1, and L2 are slightly different, the number of the affected parts is different in their own periods.

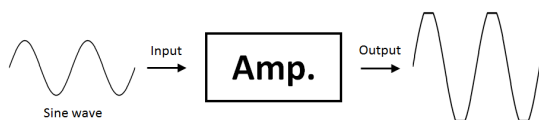


Figure 2. Conceptual figure of the amplifier saturation.

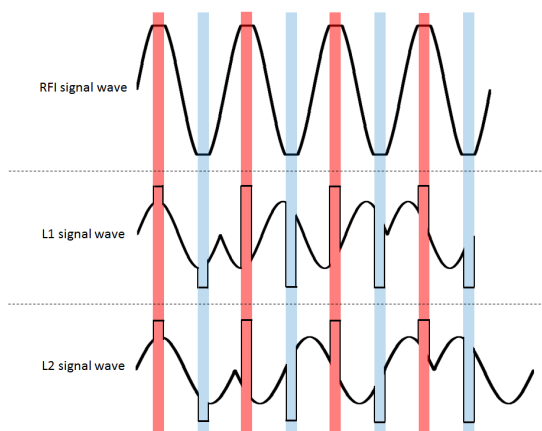


Figure 3. Schematic figure of the affected signals of L1 and L2. The parts saturated by the RFI signal are replaced with the highest values in both plus and minus sides.

In the GNSS receiver, Carrier Phase Locked Loop (CPLL) circuits are installed to reconstruct the carrier waves of GPS/QZSS signals, which are used for baseline analysis [1]. A block diagram of CPLL is depicted in Figure 4. In order to reconstruct the original carrier wave using the received carrier wave modulated by a Binary Phase Shift Keying (BPSK) technique, the square of the modulated carrier wave is generated in the CPLL circuit, and the reconstructed carrier wave is output.

If the amplifier before the CPLL circuit is saturated by the strong RFI signals, the squares of the modulated carrier wave contain high amplitude pieces quasi-periodically and the output voltage level of the Low-Pass Filter (V_{cont}) in the circuit becomes slightly higher than the normal case in order to lock the loop (Figure 5). This causes a slight shift of the frequency of the reconstructed carrier wave since the output frequency of the CPLL circuit is controlled by the voltage level of the input of the Voltage-Controlled Oscillator in the circuit. Here this phenomenon easily occurs in the case of the L1 signal because the frequency of the L1 signal is very near that of LTE. On the other hand, the frequency of the L2 signal is different from that of LTE and the CPLL circuit works as a narrow band-pass filter, so the only circuit for the L1 signal is affected.

L1 and L2 carrier phases are employed when the baseline analysis is done to determine the position of the GEONET station. Because the frequency of the L1 signal is slightly shifted when the amplifier is saturated and the shifted L1 frequency causes the periodic L1 phase bias, the height obtained as the result of the baseline analysis has a periodic offset.

More detailed mechanism is still under investigation.

4. Discussion to Solve this Problem

Because it is considered that the main cause of this problem is the amplifier saturation, it should be tried to avoid the saturation of the amplifier in the GNSS receiving system in order to solve this problem. The simplest method is insertion of an attenuator in the front of the receiver that includes the saturated amplifier. By installing attenuators with -18 dB at GEONET stations that were affected by the RFI, apparent variations became much smaller actually. The insertion of a large amount of attenuators causes the worse SNR value of the observables of L1 and L2 carrier phases. In order to avoid increase of the noise level, the total gain before the GNSS receiver (a pre-amplifier, the attenuator and cables) should be more than 30 dB.

In addition, it is expected that necessity of the

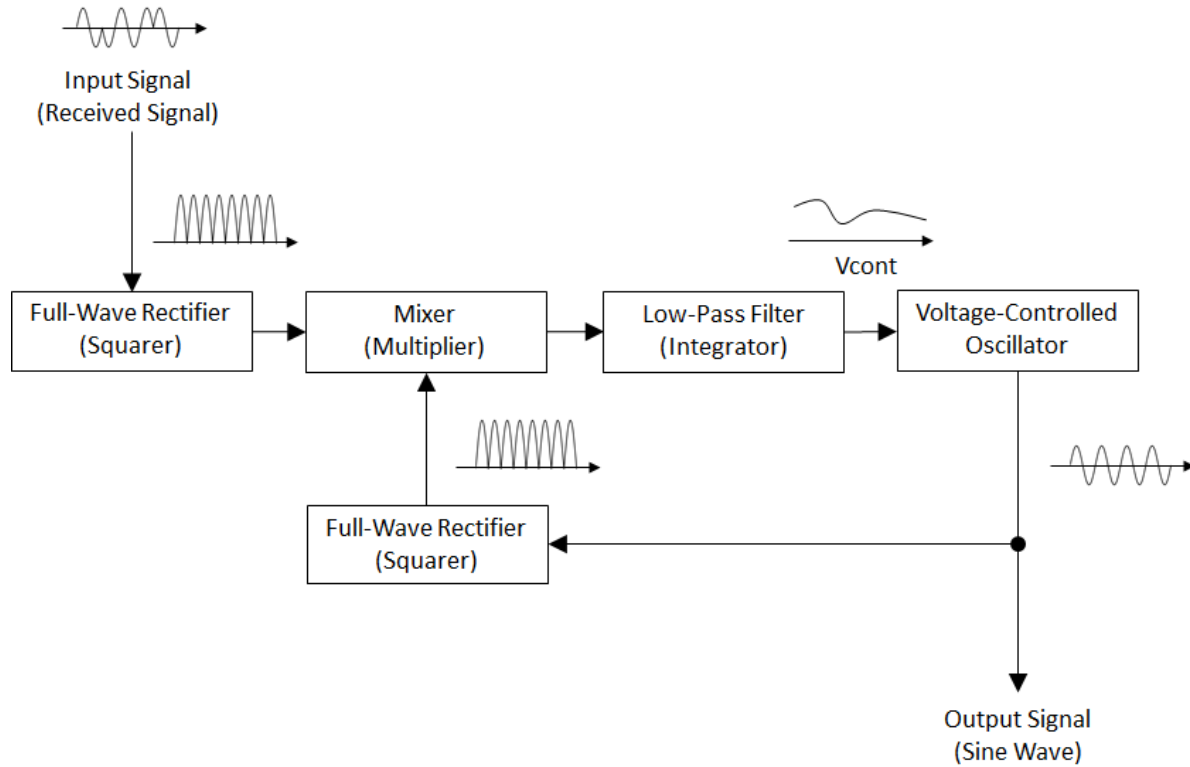


Figure 4. Block diagram of Carrier Phase Locked Loop

mobile telecommunications will increase nationwide in Japan in the near future because the mobile telecommunications is being employed to achieve the 'Internet of Things' concept. The most drastic method is to introduce the antenna and the receiver that are designed to be employed for the severe radio condition like Japan. Insertion of a filter that eliminates the frequency range for the mobile telecommunications (1.475–1.511 GHz) also seems to be available to use the present receiving system with small modification. This type of filter is called 'notch filter.' The basic specifications of the notch filter are listed in Table 1. Since the L1 frequency (1.57542 GHz) is located near the elimination frequency range, the characteristics of the filter (cut-off frequency, temperature stability, and so on) are important. Especially the phase delay characteristic is very important because the phase instability directly influences the position estimation in baseline analysis. The necessary characteristic of the cut-off frequency of the filter to design the higher frequency side is listed in Table 2 and depicted in Figure 6.

5. Summary

Because of strong RFI signals, which were originally transmitted for mobile phones, amplifier saturation occurred in the GNSS receivers, and appar-

Table 1. Basic specifications of the notch filter to eliminate mobile telecommunications signals

| Freq. (MHz) | Condition |
|-------------|------------|
| 1160–1290 | Passed |
| 1475–1515 | Attenuated |
| 1535–1590 | Passed |

Table 2. List of the necessary characteristic of the filter to design the higher frequency side

| Freq. (MHz) | Att. (dB) |
|-------------|-----------|
| 1515 | -60 |
| 1516 | -55 |
| 1518 | -47 |
| 1520 | -38 |
| 1523 | -25 |
| 1525 | -18 |
| 1528 | - 8 |
| 1530 | - 3 |
| 1535 | 0 |

ent height variations of several GEONET stations with a specific receiver were detected. Although

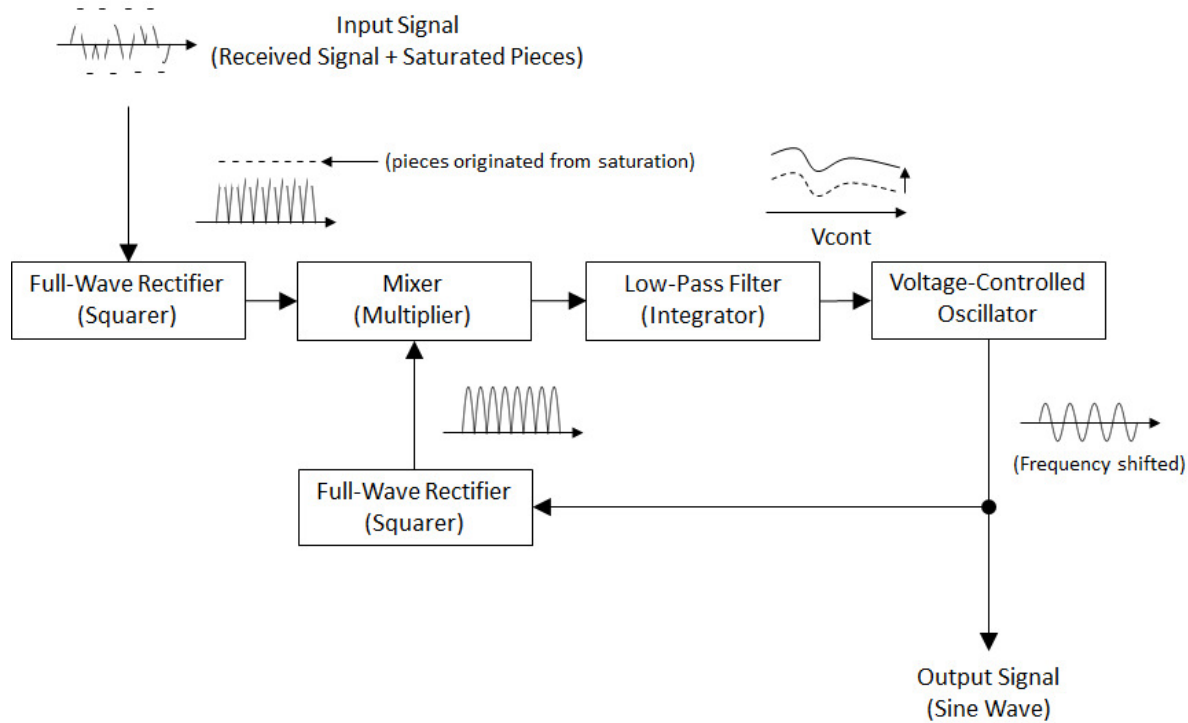


Figure 5. Explanation of the frequency shift caused by the saturated signal in PLL. High amplitude pieces originated from the saturation cause the shift of V_{cont} , which makes the output frequency shifted.

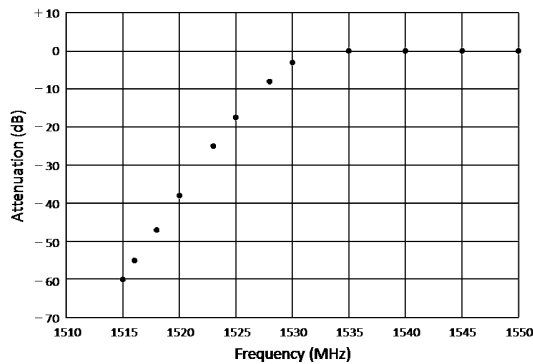


Figure 6. Graph of the necessary characteristic of the filter to design the higher frequency side

its generation mechanism was still not clear, the apparent variations became much small by inserting the attenuator to avoid the amplifier saturation in the GNSS receiver. The detail of the generation mechanism of the apparent height variations is still under investigation.

6. Acknowledgments

The authors would like to thank GSI's colleagues who have worked for the RFI problem at GEONET stations.

References

- [1] Geodetic Society of Japan, GPS –Precise Positioning System using Satellites–, 1986, published by the Japan Association of Surveyors (in Japanese).

Look back on 18 years of Tsukuba 32-m antenna

Midori FUJIWARA

(fujiiwara-m96qu@mlit.go.jp),

Shinobu KURIHARA, Masayoshi ISHIMOTO, Takahiro WAKASUGI, Michiko UMEI

*Geospatial Information Authority of Japan,
1 Kitasato, Tsukuba Ibaraki, Japan*

Abstract: The Geospatial Information Authority of Japan (GSI) has implemented VLBI operation in order to determine the precise position of Japan on the earth and to monitor plate motion in and around Japan since 1984. Tsukuba 32-m VLBI antenna which was built in 1998 was a leading VLBI antenna in the world, and contributed to the rapid determination of earth orientation parameter (EOP) in cooperation with foreign observatories under the International VLBI Service for Geodesy and Astrometry (IVS) and the revision of the Japanese Geodetic Datum after the 2011 off the Pacific coast of Tohoku Earthquake. In this article, Tsukuba's several contributions are reviewed.

1. Introduction

From 1998 through 2002, GSI used to implement VLBI operation by using Kashima 26-m antenna owned by the Radio Research Laboratory (at present The National Institute of Information and Communications Technology; NICT). When the Japanese Geodetic Datum 2000 (JGD2000) was realized, the coordinates of more than 110 thousand of control points in all over Japan were calculated based on the position of Kashima 26-m antenna which was derived from its international VLBI observations. Then Kashima 26-m antenna built in 1968 was replaced by Tsukuba 32-m antenna of which construction budget was approved in the 2nd supplemental budget for the Great Hanshin-Awaji Earthquake in 1995 (Tsuji *et al.*, 2004). Table 1 shows the specification of Tsukuba 32-m antenna. Its design was optimized for geodetic observation, and it had a large parabolic dish and Azimuth/Elevation motors to slew the antenna quickly. Therefore, it could acquire high quality data efficiently.

2. The chief events of Tsukuba 32-m antenna

The chief events of Tsukuba 32-m antenna for 18 years are shown in Table. 2 Tsukuba 32-m antenna was involved in about 2,600 sessions in 18



Figure 1. View of the Tsukuba antenna.

Table 1. Tsukuba specifications (Wakasugi *et al.*, (2015))

| | |
|----------------------------|-----------------|
| Year of construction | 1998 |
| Radio telescope mount type | Az-El |
| Antenna optics | Cassegrain |
| Diameter of main reflector | 32 m |
| Az/El drive velocity | 3°/sec |
| SEFD(X/S) | 320 Jy/360 Jy |
| Frequency range (S-band) | 2.10 ~ 2.50 GHz |
| Frequency range (X-band) | 7.78 ~ 8.98 GHz |

years from 1998 through the end of 2016. At the beginning of its operation, the open-reel type magnetic tapes called Mark4 system for international observations, and the cassette cartridge type magnetic tapes called K4 system for domestic observations were used as recording media. The Mark4 system needed a few manual tape changes in one 24-hr observation. From around 2005, the magnetic tapes have taken the place of the pc-based data acquisition system with hard disk drives (K5 system). As a result of this replacement, the manual tape change became unnecessary, and the automatic unmanned operation and data transfer via network became possible. This caused the increase of the number of sessions per year from around 100 in the magnetic tape era to around 200. The K5 system and data transfer via network produces a new VLBI application. The actual measurement of UT1-UTC is practically and technically possible by only VLBI, however, for its rapid determination, a long latency of VLBI, which is caused by data transfer and correlation processing, had been a consideration for a long time. GSI, NICT, Onsala Space Observatory in Sweden, and Metsähovi Radio Observatory in Norway worked on an experiment for rapid determination of UT1-UTC, and automated the whole process from data transfer through analysis. In February 2008, we derived

Table 2. The chief events of Tsukuba 32-m antenna.

| | |
|---------|---|
| 1998.3 | Antenna construction was completed. |
| 1998.6 | First international experiment was carried out. |
| 2002.5 | Intensive UT1 session series was started. |
| 2000.5 | K4/Mark4 systems were replaced by K5 system completely. |
| 2003.5 | The experiments for the orbit determination of the space probe 'Hayabusa' (Joint research with Japan Aerospace Exploration Agency (JAXA)/ Institute of Space and Astronautical Science (ISAS)) |
| 2005.9 | The IVS 15-day campaign session CONT05 was implemented. (Followed by CONT08, CONT11, and CONT14.). |
| 2008.2 | GSI and NICT succeeded in measurement of UT1-UTC within only 3 min 45 sec after the end of the session. |
| 2011.5 | GSI revised the coordinates of 438 CORS stations in east Japan due to the crustal deformation caused by the 2011 off the Pacific coast of Tohoku Earthquake. These coordinates were calculated based on VLBI observations during one month just after the earthquake. |
| 2014.3 | Ishioka VLBI station was completed. |
| 2016.12 | The final international experiment was done. |
| 2017.3 | Dismantlement of Tsukuba 32-m antenna ended. |

UT1-UTC from the experiment in 3 min 45 sec from the end of the observation. (Kurihara and Kokado, 2009). On the other hand, Tsukuba 32-m antenna contributed to the realization of the national geodetic reference frame after the 2011 off the Pacific coast of Tohoku Earthquake. The earthquake caused the large crustal deformation over a wide area of Eastern Japan. The coordinates of national control points such as Continuously Operating Reference Station (CORS) and triangulation points in the area became unavailable due to the crustal deformation. Though Tsukuba 32-m antenna put off restarting the VLBI operation after the earthquake for a while due to aftershocks with an intensity of lower 5 or greater on the Japanese seismic scale, on April 4th Tsukuba came back to the international observation. On May 31st GSI revised and published the new coordinates of 438 CORS stations. The coordinates of these stations were calculated based on the international VLBI observation at Tsukuba on May 10. (Hiyama et al., 2011).

3. Dismantlement

In 2009, a Committee of IVS showed the new specification of next generation VLBI system called VLBI Global Observing System (VGOS) (Petra-chenko et al., 2009). The committee said that the current VLBI system will be replaced by VGOS in



Figure 2. The process for destroying the antenna. (1) Removing the main reflector. (2) After detaching the main reflector and sub reflector. (3), (4) Detaching the center hub by cutting into small parts by gas cutting method. (5) The frameworks were dismantled. (6) The site after dismantlement of the antenna.

future. Thus, it was necessary for GSI to build the new VGOS-compliant VLBI antenna in order to continue maintaining the precise position of Japan on the global geodetic reference frame. The government of Japan approved the establishment of the VGOS antenna system for enhancement of monitoring crustal deformation including plate motions in global scale on the supplemental budget for the Great Tohoku Earthquake. The new VGOS station was completed in 2014 at Ishioka, Ibaraki and had been implemented parallel observation until the end of 2016 with Tsukuba 32-m antenna for smooth succession of the result of Tsukuba. GSI decided the future VLBI operation with one observatory Ishioka. It meant that Tsukuba 32-m antenna was dismantled and removed. The dismantlement started from January 2017. The main reflector, the sub reflector, and center hub of the main reflector were detached in this order from the main body of the antenna (Fig. 2). The dismantlement ended at the end of March 2017

4. Conclusion

This report briefly reviewed the 18-year history of Tsukuba 32-m antenna. It participated in many sessions and contributed to monitoring earth orientation and crustal deformation as well as maintaining geodetic reference frame. Through the operations, the know-hows of operations, such as automated operation, data transfer and stable observation with less failure were accumulated. Such know-hows are utilized in the operation of Ishioka VLBI antenna.

Hiyama, Y., A. Yamagiwa, T. Kawahara, M. Iwata, Y. Fukuzaki, Y. Shouji, Y. Sato, T. Yutsudo, T. Sasaki, H. Shigematsu, H. Yamao, T. Inukai, M. Ohtaki, K. Kokado, S. Kurihara, I. Kimura, T. Tsutsumi, T. Yahagi, Y. Furuya, I. Kageyama, S. Kawamoto, K. Yamaguchi, H. Tsuji, S. Matsumura, "Revision of the Results of Control Points after the 2011 off the Pacific coast of Tohoku Earthquake", Bulletin of the Geospatial Information Authority of Japan, 59, 2011.

Kurihara, S., Kokado, K., "Ultra-Rapid UT1 Experiment Using e-VLBI Technique", Bulletin of the Geospatial Information Authority of Japan, 57, 2009

Petrachenko, B., A. Niell, D. Behrend, B. Corey, J. Böhm, P. Charlot, A. Collioud, J. Gipson, R. Haas, T. Hobiger, Y. Koyama, D. MacMillan, Z. Malkin, T. Nilsson, A. Pany, G. Tuccari, A. Whitney, J. Wresnik, "Design Aspects of the VLBI2010 System", Progress Report of the IVS VLBI2010 Committee, 2009.

Tsuji, H., T. Tanabe, H. Kawawa, K. Takashima, K. Miyagawa, S. Kurihara, S. Matsuzaka, "Achievements of Outgoing Kashima 26m VLBI Antenna for Geodesy and Surveying; Journal of the Geospatial Information Authority of Japan, 103, 2004. (in Japanese)

Wakasugi, T., R. Kawabata, S. Kurihara, Y. Fukuzaki, J. Kuroda, K. Wada, S. Mizuno, T. Ishida, "Tsukuba 32-m VLBI Station", International VLBI Service for Geodesy and Astrometry 2014 Annual Report, 2015.

Phase-up Twin Antennas for High-Sensitivity Maser Observations

Kazuhiro Takefuji¹ (*takefuji@nict.go.jp*)
 Koichiro. Sugiyama², Yoshinori Yonekura³,
 Tagiru Saito⁴, Kenta Fujisawa⁵, and
 Tetsuro Kondo¹

¹ *Kashima Space Technology Center, National Institute of Information and Communications Technology, 893-1 Hirai, Kashima, Ibaraki 314-8501, Japan*

² *Mizusawa VLBI Observatory, National Astronomical Observatory of Japan, 2-21-1 Osawa, Mitaka, Tokyo 181-8588, Japan*

³ *Center for Astronomy, Ibaraki University, 2-1-1 Bunkyo, Mito, Ibaraki 310-8512, Japan* ⁴ *College of Science, Ibaraki University, 2-1-1 Bunkyo, Mito, Ibaraki 310-8512, Japan* ⁵ *The Research Institute for Time Studies, Yamaguchi University, 1677-1 Yoshida, Yamaguchi, Yamaguchi 753-8511, Japan*

Abstract: For the sake of high-sensitivity 6.7 GHz methanol maser observations, we developed a new technology for coherently combining the two signals from the Hitachi 32 m radio telescope and the Takahagi 32 m radio telescope. Furthermore, we have applied newly developed digital position switching (DPS), which is a similar technology to that used in noise-cancelling headphones, and we confirmed the improvement the sensitivity of DPS rather than that of the VLBI method. See more detail in Takefuji et al., 2017.

1. Introduction

The establishment of a synthesis technology using two signals from two stations with a maser observation as a reference is our first goal. Once this technology is realized, the phase difference of the synthesis parameters can be determined by the maser observation with two antennas. As a result, the observation efficiency is expected to be improved. Moreover, in the case of spectral observation, the position switching of a single dish is performed by moving the antenna physically. Then, the system noise and other background noises can be removed and only the maser signal will remain. Once two antennas are phased, it is expected to create a virtual-off source by changing the phase of the synthesis parameters similarly to noise-cancelling headphones. Without physically moving the antenna, the digital position switching observation

is considered to be performed. This is the second goal of our research. Thus, we attempt to use the above techniques with the Hitachi 32 m radio telescope and the Takahagi 32 m radio telescope of the Japanese VLBI network (JVN), which are separated by about 260 m. Furthermore, we perform VLBI experiments simultaneously with the Kashima 34 m radio telescope at a distance of about 50 km and the Yamaguchi 32 m radio telescope at a distance of about 1000 km to confirm the improved sensitivity of a combined signal.

2. Parameters for phasing two radio telescopes by maser observation

If we define P_a as the signal power of antenna A and P_b as the signal power of antenna B, then P_{sum} , the signal power after combining antennas A and B with phase difference $\Delta\theta$, can be expressed as

$$P_{sum} = |P_a + P_b| \quad (1)$$

$$= \sqrt{P_a^2 + P_b^2 + 2P_aP_b \cos \Delta\theta}. \quad (2)$$

The maximum value of the combined signal is $P_a + P_b$ and the minimum value is $P_a - P_b$ (when $P_a \geq P_b$). If the signal powers of the two antennas are equal, the power is doubled. However, depending on the phase difference $\Delta\theta$, the signal will decrease and disappear in the worst case. The extinction state can be used as an off-source observation. By adding an offset of 180° to the perfectly matched angle $\Delta\theta$, it can be applied for digital position switching.

By focusing on the phase, the rotation of the phase difference $\Delta\theta$, which is caused by the delay difference between the two antennas, shifts very rapidly in our experiment. The predicted values such as the geometric delay and delay rate are calculated using a VLBI software in advance and are reasonably accurate. However, it is necessary to determine the phase difference between the antennas by actual observation. On the other hand, the bandwidth covering maser emission is generally on the order of 100 kHz. Therefore, the accuracy of the delay determined by interferometry is not so high. In addition, if the phase at the frequency of the peak intensity of the maser emission in the cross-spectrum is determined, it has to be converted to the phase at the sky frequency, i.e. the phase at 0 MHz of the intermediate frequency (IF). In this conversion, the precise delay information is also required. It is difficult to synthesize the signals of two telescopes without any corrections of the phase difference.

Here, we will determine the phase difference $\Delta\theta$ by the following procedure. Firstly, we observe

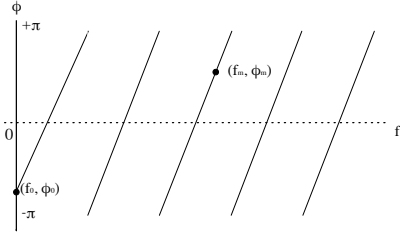


Figure 1. Relationship of the initial phase difference ϕ_0 at the sky frequency f_0 and the phase difference ϕ_m at the maser emission line f_m against an intermediate frequency on cross-spectrum after a correlation. The discontinuous solid lines with the slope of $2\pi\tau_g$ represent the delay τ_g between two telescopes determined beforehand by the observations of the radio continuum sources.

a strong quasar to determine the clock offset between two antennas. If the reference clocks of the telescopes are the same, the difference in the clock rate between the telescopes is small. Otherwise, it would be better to observe the quasars in the latter scan to estimate the clock rate. Secondly, we observe a series of maser sources with the two telescopes. Thirdly, we correlate the recorded data between the two telescopes whose geometric or clock delay were adjusted to be identical so that the phase difference $\Delta\theta$ was involving the whole delay. Finally, we convert the obtained phase difference $\Delta\theta$ at the maser line to the phase at the sky frequency.

Figure 1 shows a conceptual phase on a cross-spectrum after performing a cross-correlation for the phase conversion. A maser emission line is present at the frequency and the fringe phase (f_m, ϕ_m) at the sampling frequency of f_{sps} [Hz]. The initial phase at the sky frequency (f_0, ϕ_0) is required to synthesize two telescopes. Here, the total delay comprising the geometric and clock delays is represented as the discontinuous slopes due to an ambiguity of 2π of the cross-spectrum. Now, we define the total delay as τ_g [s] and the initial phase is expressed as

$$\phi_0 = \phi_m - 2\pi f_m \tau_g \pmod{2\pi}. \quad (3)$$

In contrast to the continuum source observation, the phase can be determined only at the frequencies where the maser emission exist. Therefore, discontinuous slopes in Fig. 1 do not appear, so that it is difficult to convert ϕ_m into ϕ_0 . However, once the delay τ_g is obtained by the previous quasar observation, it becomes possible to determine ϕ_0 from

ϕ_m using Eq. 3. In addition, the delay rate can be determined by tracking the phase ϕ_m of the maser emission line. Thus, the parameters for phasing two telescopes can be obtained.

Figure 2 shows a schematic diagram of the phased telescopes. Firstly, the Fourier transform is performed for two signals from the two telescopes and then the delay with reference to the antenna A is corrected in the frequency domain. We actually performed a 2048-length fast Fourier transform (FFT) for the signals of Hitachi and Takahagi. After the FFT, the obtained phase, delay, and delay rate were corrected in a frequency domain. The signal of the antenna B at this time can be regarded as observed at the position of the antenna A. Thereafter, signals were synthesized and returned to the time-series data by inverse FFT (2048 points). Finally, the combined signal was generated.

3. Observations

We carried out the maser observation from 03:47 to 16:32 (UTC) on 26 Oct 2016 (DOY 300). Before the maser observation, we observed the quasar NRAO512 to determine the geometric and clock delays among telescopes and performed a series of maser observations. The telescopes used in each observation are described in table 1. The band-filtered radio frequency (RF) signals (from 6664 to 6672 MHz) of antennas were down-converted and the intermediate frequency (IF) signals (from 0 to 8 MHz) were sampled by using the analogue to digital sampler K5/VSSP32 with a 16 MHz sampling speed and 4-bit quantization

4. Results

4.1 Phased telescopes

In accordance with the aforementioned procedure, we observed a total of 56 masers using the Hitachi and Takahagi telescopes as the phased antennas. The recorded data of the Takahagi 32m telescope were shifted to those of the Hitachi 32m telescope position. Figure 3 shows the spectra of the maser source G26.52-0.26 with the phased and unphased antennas with 60 s integration and 1 kHz resolution. We removed the trends of the band-pass profiles by the least-squares method with a quadratic function and give the offset for comparison. The SNRs of each spectrum were estimated to be about 6.4, 4.8, and 4.6 from top to bottom.

By adding an offset of 180° to the perfectly matched phase of the phased antenna, it can be considered as a virtual off-source and applied for digital position switching. If digital position switching is realized, the off-source observations can be skipped and therefore it is expected that

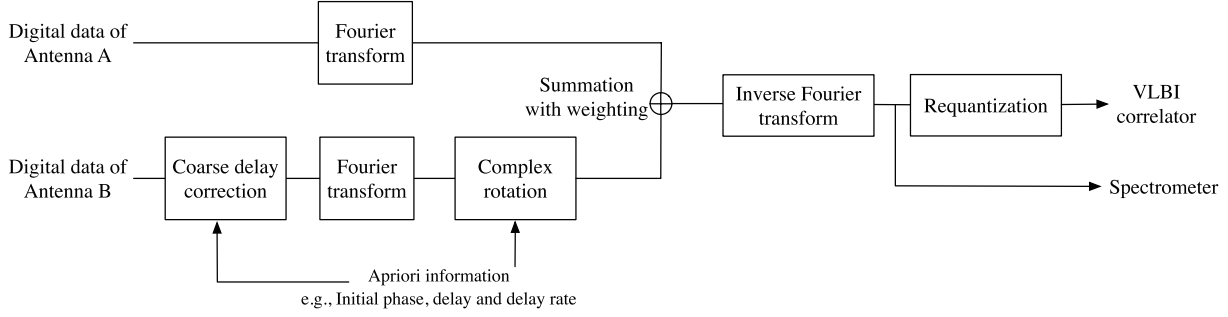


Figure 2. Schematic diagram of the procedure of the phased telescopes.

Table 1. Parameters of the experiment ($f_c = 6668$ MHz) on 26 Oct 2016 (DOY 300).

| Station | Hitachi | Takahagi | Kashima | Yamaguchi |
|------------------------|------------------|-----------|----------|-----------------|
| Diameter [m] | 32 | 32 | 34 | 32 |
| T_{sys}^* [K] | 29.5(@EL=85 deg) | Typ 30-40 | Typ 150 | 110(@EL=46 deg) |
| Efficiency [%] | 55-75 | 55-75 | Typ 40 | Typ 65 |
| Polarization | LHCP | LHCP | Vertical | LHCP |
| Weather | Fine | Fine | Fine | Cloudy |

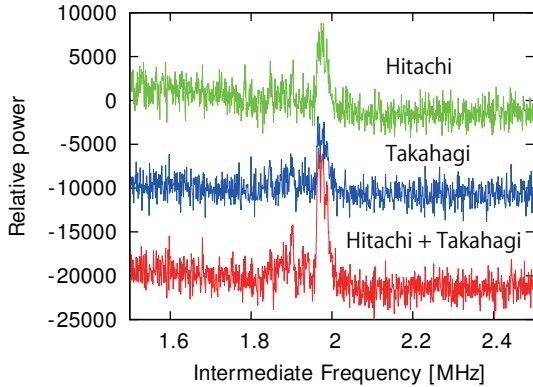


Figure 3. Spectra of the maser source G26.52-0.26 obtained by the Hitachi telescope (top), by the Takahagi telescope (middle) and by the phased Hitachi and Takahagi telescopes (bottom).

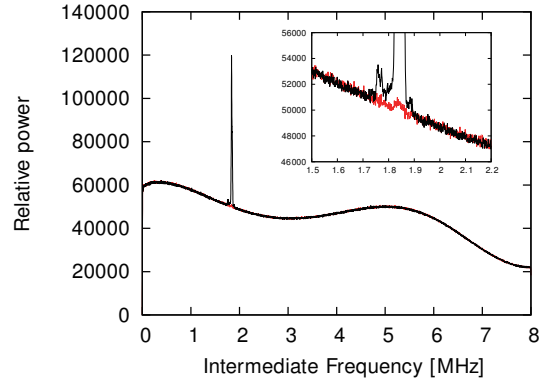


Figure 4. The on-source and the off-source spectra of maser G12.025-0.031 calculated by the digital position switching of the phased Hitachi and Takahagi antennas.

the observation efficiency will be increased. Figure 4 shows the ON-OFF spectra calculated using the phased Hitachi and Takahagi antennas. The on-source data contains the maser signal of G12.025-0.031 for the in-phase combination with 60 s integration and 1 kHz resolution. On the other hand, the off-source data is obtained by suppressing the maser signal by applying a phase difference of 180° to the in-phase combination. From the figure, the band characters without the maser region have the same curvature and were consistent between the on-source and the off-source. Here, we provided a single parameter for the phasing procedure. The

amplitude of the on-source can be increased owing to the more accurate accumulation. Figure 5 is obtained by multiplying the ratio (ON-OFF)/OFF by the system equivalent flux density (SEFD), which we assumed to be 85 Jy. Since the SEFD of both the Hitachi and Takahagi telescopes is approximately 170 Jy, when the efficiency and the system temperature are 70% and 30 K, respectively, we provided the half value of the SEFD. Here, the obtained flux density of the maser sources is consistent with our recent monitoring result. Since the power, when the maser did not exist, is close to zero, the common components such as the band character were removed.

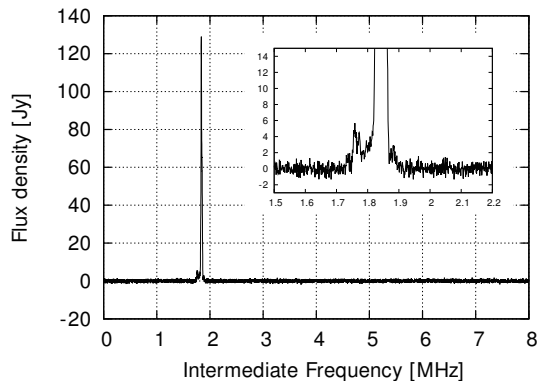


Figure 5. Spectrum formed from the ratio (ON-OFF)/OFF of maser G12.025-0.031.

Finally, Fig. 6 shows a comparison of the SNRs of the detected maser sources with 60 s integration obtained using VLBI and the phased telescope. Only the data whose SNR was over 15 were plotted. The mean SNR of the phased antenna relative to that of VLBI is 1.597 ± 0.444 . In the calculation of the SNR, the 1σ noise was commonly defined for both methods from the scan, in the frequency range where no maser lines were detected. Then, the SNR was obtained by dividing the peak power of the maser line by the defined σ . The spectra obtained by the digital position switching were produced without the requantization effect. Thus, the obtained SNRs could be directly compared. Since some maser scans had a factor of 2 or 3 unexpectedly, the results may have been overestimated (the median of the SNR ratio was 1.410). We assume that the radio continuum emission toward the maser source is one possibility.

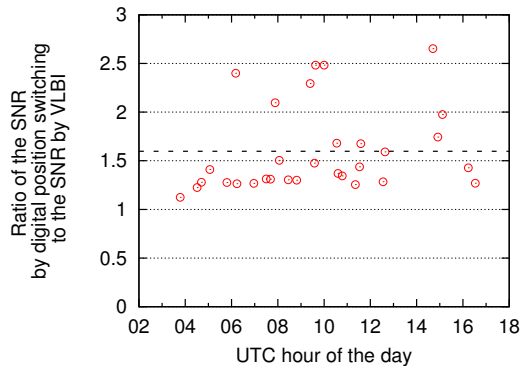


Figure 6. Comparison of the maser SNR of VLBI and the phased telescopes of Hitachi 32 m and Takahagi 32 m as a function of time. The SNRs by the VLBI method were extracted from the cross-spectrum of the VLBI made for the Hitachi and Takahagi telescopes. While, the SNRs by the phased method were obtained by the spectrum of digital position switching (ON-OFF) with the phased two telescopes of Hitachi and Takahagi telescopes. The mean SNR ratio of the phased antenna relative to that of VLBI is 1.597 ± 0.444 (dashed line) and the median of the SNR ratio is 1.410.

5. Summary

We developed phased-up technology using the twin antennas Hitachi and Takahagi and applied it to a series of 6.7 GHz methanol maser observations. Furthermore, with the newly developed digital position switching, we confirmed that the phased telescopes operated over 12 hours with a maser observation as a reference without any off-source observations. Thus, the off-source observations can be skipped and therefore we expect that the observation efficiency will be increased.

References

- [1] Takefuji, K. et al., “Development of the Phase-up Technology of the Radio Telescopes: 6.7 GHz Methanol Maser Observations with Phased Hitachi 32 m and Takahagi 32 m Radio Telescopes”, PASP, Vol 129, No 981, 2017

Development of Wideband Antenna

Hideki Ujihara (ujihara@nict.go.jp)

Kashima Space Technology Center,
National Institute of Information
and Communications Technology,
893-1 Hirai, Kashima, Ibaraki 314-8501, Japan

1. Status of development

The prototype of NINJA feed installed in the Kashima 34m antenna in 2015 was replaced with a new NINJA feed developed for 34m. Previous model was composed with a NINJA feed designed for the primary focus of the previous MARBLE with a 1.5m or 1.6m parabola dish. The new feed was shortened and designed for 3.2-14.4 GHz with reduced waveguide dimensions to set cutoff frequency around 3 GHz, and was mounted again nearby the IGUANA Daughter feed which is operated in 6.5-15 GHz band[1] as shown in Figure 2. Also a orthogonal mode transducer(OMT) was developed for the new feed for capability of receiving for both two linear polarizations. The main reflector of MARBLE 1 at AIST Tsukuba was enlarged from 1.6 m to 2.4 m and its optics was changed to the Cassegrain with the NINJA in the same way for MARBLE 2 at NICT Koganei, as shown in Figure 3. CFRP pipes are used to support the sub reflector instead of aluminium frames to reduce the total load on the antenna mount. They are operated with 20-40 % aperture efficiency with OMT.

2. Plans

New wideband OMT and NINJA feeds were developed for better performance, but RFI below 3GHz is not cut well for Kashima 34 m that causes

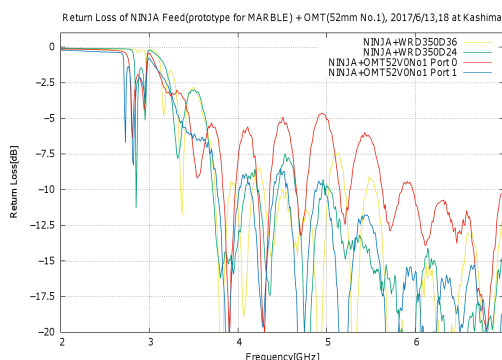


Figure 1. Return loss measurement of the new wideband OMT with the NINJA feed.



Figure 2. The NINJA feed and the IGUANA feed in the Kashima 34m receiver cabin.



Figure 3. MARBLE 2.4m on the roof top of the AIST Tsukuba.

modulation noise to increase T_{sys} over 200K. So further development will be done for OMT and NINJA feeds. Also, wideband OMTs will be developed for the IGUANA feeds. Frames of MARBLE 2 will be replaced with CFRP pipes to reduce the mass and to gain rigid surface of the main reflector.

References

- [1] Ujihara H., (2016) Development of wideband feed for Kashima 34m Antenna, Radio Sci., 52, doi:10.1002/2016RS006071

'Node - HUB' Style VLBI with Broadband System.

Mamoru Sekido (*sekido@nict.go.jp*), NICT

Space-Time Standards Laboratory,
Kashima Space Technology Center,
893-1 Hirai, Kashima Ibaraki, Japan

Abstract: Our VLBI project is targeting distant frequency comparison with broadband VLBI system. Transportable small VLBI stations are used as the nodes of the measurements, and large diameter antenna is participating the VLBI observation as a hub for boosting signal to noise ratio. Delay observable between small antenna pair is not always expected to be directly measured by VLBI, but indirectly derived by using closure delay relation including large diameter antenna. This observation scheme was not attractive because of larger error in the past. Although it obtained a reality to be used in geodesy by high delay precision with broadband VLBI. Because broadband VLBI can achieve sufficiently high delay precision even with small diameter antenna. We named this observation scheme as 'Node - Hub style (NHS) VLBI', in which multiple small antennas work as the nodes and small number of large diameter antennas work as hub to enhance the SNR. The NH VLBI will has some advantages in geodetic VLBI and frequency transfer VLBI application. This paper describes algorithm and some aspect of the NHS VLBI scheme.

1. Introduction

VLBI group of NICT have been working for application of broadband VLBI system to frequency comparison between distant atomic frequency standards [1]. The concept of broadband VLBI system VGOS [2] has been proposed by the IVS, and its prototype system so called NASA Proof of Concept (PoC) is current standard of the VGOS system. Our broadband data acquisition system named GALA-V is another realization of the VGOS. By implementation of originally developed broadband feed [3, 4], Kashima 34m antenna and two small Cassegrain antennas have gained broadband observation capability. The GALA-V system employed a unique data acquisition technique so called RF-Direct sampling[5], which assisted precise broadband group delay measurements by wide bandwidth synthesis software [6]. Combination use of small diameter antennas as nodes and high sensitivity antenna as a hub is another aspect of our VLBI project.

Concept of transportable small VLBI station has been investigated since 1980s to expand the capability of VLBI in global geodesy [7, 8, 9]. At present the German Geographical Authority BKG has been operating 6-m diameter VLBI station TIGO[10]

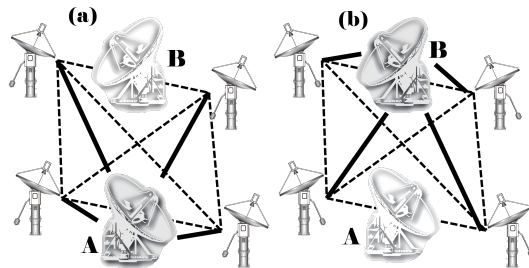


Figure 1. Multiple small diameter antennas are the nodes of observation and they makes VLBI observation with large diameter antenna 'A' in one scan (panel (a)). Small antennas can quickly change radio source for the next scan, and antenna 'B' is used for hug of the next scan (panel (b)), which is prepared during previous scan. And antenna 'A' will move to the next scan while antenna 'B' is observing the current scan. In this way, large antennas 'A' and 'B' participate observation alternately, and they play the role of hub in the network to enhance the SNR. Delay observables between small antenna pairs are derived from delay observables of node and hub baselines by closure delay relation. This procedure has several benefits as described in text.

in South America, which is a geodetic complex equipped with multi space geodetic techniques.

Even though a small diameter antenna can work as a geodetic VLBI station by combination observation with larger antennas, its delay precision has been limited by the signal to noise ratio (SNR) in legacy S/X observation. This situation has been changed in broadband VLBI case. As we see in latter section, precision of group delay measurement was drastically improved by synthesizing the signal over broad frequency range. Fringe detection is still matter by sensitivity, although if fringe is detected, small VLBI station works as geodetic VLBI station with sufficient geodetic precision.

The SNR of VLBI observation is proportional to square root of data acquisition rate and the products of diameters (sensitivity) of the two telescopes of the baseline, VLBI sensitivity can be improved by higher data acquisition rate and joint observation with large diameter (higher sensitivity) antenna.

Let us suppose multiple small diameter stations and some high sensitivity stations are available for VLBI network observation (Fig. 1). Small stations are regarded as node, whose position and clock parameters are to be measured. Large diameter high sensitivity stations play the role of hub to enhance the SNR of observation. Small antenna can move fast, then it can change observing radio source quickly. Large diameter antenna will not move so fast, although it has high sensitivity. We propose a new VLBI observation scheme, which takes these

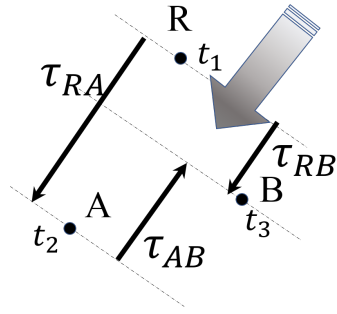


Figure 2. A wave-front of signal from a target radio source is arriving to Station R, A, and B at t_1 , t_2 , and t_3 , respectively.

advantages of merits of both small and large diameter antennas. Small antennas (nodes) play the key role in the measurement, where many radio sources are observed in a unit of time by quickly changing radio sources. At least one large antennas (hubs) must be included in the network observation to enhance the SNR of node stations network. All the large diameter antenna need not participate all the time, but they may participate alternatively. Appropriate scheduling will enable to keep enough time for large diameters (hub) antenna to move large angular distances for the next scan while the other hub antenna is participating current scan. In this case, sufficient SNR may not be gained for the small antenna (nodes) pairs. Thus, delay observables between small station (nodes) pairs are derived from delay observables of node-hub baselines by using closure delay relation. We named this observation scheme as Node-Hub style (NHS) VLBI.

2. The NHS VLBI observation scheme

2.1 Closure Delay

Utilizing virtual delay between node stations derived from node-hub baselines by using closure delay relation is unique technique of the NHS VLBI. Closure delay relation is schematically depicted in Fig. 2. Let us suppose three stations are observing a common radio source, and a wave-front of radio signal from the target radio source is arriving to station R, A, and B at epoch of terrestrial time t_1 , t_2 , and t_3 , respectively. Here we define propagation delay as $\tau_{XY}^{\text{prop}} = \tau_{XY}^{\text{geo}} + \tau_{XY}^{\text{atm}}$, which is sum of signal propagation delay due to geometry of XY baseline and propagation in the atmospheric including ionosphere. Propagation delays are expressed as signal arrival time difference, then propagation delays between three stations are represented as follows:

$$\left. \begin{aligned} \tau_{RA}^{\text{prop}}(t_1) &= t_2 - t_1 \\ \tau_{AB}^{\text{prop}}(t_2) &= t_3 - t_2 \\ \tau_{BR}^{\text{prop}}(t_3) &= t_1 - t_3 = -\tau_{RB}^{\text{prop}}(t_1) \end{aligned} \right\}, \quad (1)$$

where delay τ_{XY} is defined at reference epoch, when the signal arrivals to station X. Summation of three

equations of (1) becomes

$$\tau_{AB}^{\text{prop}}(t_2) = \tau_{RB}^{\text{prop}}(t_1) - \tau_{RA}^{\text{prop}}(t_1). \quad (2)$$

Since current VLBI analysis software CALC/SOLVE[11] treat delay data of any baselines in identical scan at a common integer second epoch, then the reference epoch must be adjusted to the epoch t_1 , which is the reference integer second epoch of this scan. By using $t_2 = t_1 + \tau_{RA}^{\text{prop}}$ of eqn (1), delay of AB baseline at epoch t_2 is expressed by Taylor series expansion of $\tau_{AB}(t)$ around epoch t_1 as

$$\tau_{AB}^{\text{prop}}(t_2) = \tau_{AB}^{\text{prop}}(t_1) + \sum_{i=1}^{\infty} \frac{d^i}{dt^i} \tau_{AB} \cdot (\tau_{RA}^{\text{prop}})^i. \quad (3)$$

Then we get

$$\begin{aligned} \tau_{AB}^{\text{prop}}(t_1) &= \tau_{RB}^{\text{prop}}(t_1) - \tau_{RA}^{\text{prop}}(t_1) \\ &- \frac{d}{dt} \tau_{AB} \cdot \tau_{RA}^{\text{prop}} - \frac{d^2}{dt^2} \tau_{AB} \cdot (\tau_{RA}^{\text{prop}})^2 - \dots \end{aligned} \quad (4)$$

Note that theoretical a priori delay value τ_{RA}^{prop} and its derivative must be used, but not observed delay τ_{RA}^{obs} , for the correction term of eqn (4). Because observed delay τ_{RA}^{obs} may contain clock offset of a few μsec . Thus, it does not correctly represent propagation delay. Theoretical a priori delay has precision no worth than 1×10^{-8} sec. by using good a priori model such as CALC [11]. In this case, magnitude of the second order term of eqn (4) becomes less than 3×10^{-14} on any ground based baseline, thus higher order correction terms can be safely eliminated.

Delay observable of RA baseline is composed of contribution of propagation delay including geometry and atmosphere (τ_{RA}^{prop}), station dependent delay including clock and instrumental (τ_{R}^{stn} , τ_{A}^{stn}), and delay caused by radio source structure (τ_{RA}^{str}).

$$\tau_{RA}^{\text{obs}} = \tau_{RA}^{\text{prop}} + \tau_{A}^{\text{stn}} - \tau_{R}^{\text{stn}} + \tau_{RA}^{\text{str}}, \quad (5)$$

where time argument (t_1) is omitted for simplicity. Radio source structure effect of group delay is derivative of visibility phase with respect to the radio frequency [12]. Visibility of VLBI is obtained by integration of interferometry fringe weighted by brightness distribution of radio source on the sky, thus it depends on radio source brightness distribution and the projected baseline.

Then taking difference of delays between RA and RB baselines with eqn (5) becomes

$$\begin{aligned} \tau_{RB}^{\text{obs}}(t_1) - \tau_{RA}^{\text{obs}}(t_1) &= \tau_{RB}^{\text{prop}}(t_1) - \tau_{RA}^{\text{prop}}(t_1) \\ &+ \tau_{B}^{\text{stn}} - \tau_{A}^{\text{stn}} + \tau_{RB}^{\text{str}} - \tau_{RA}^{\text{str}}. \end{aligned} \quad (6)$$

Expecting delay observable of AB baseline corresponding to eqn (5) is

$$\tau_{AB}(t_1)^{\text{obs}} = \tau_{AB}^{\text{prop}}(t_1) + \tau_{B}^{\text{stn}} - \tau_{A}^{\text{stn}} + \tau_{AB}^{\text{str}} \quad (7)$$

By eliminating $(\tau_{RA}^{prop}(t_1), \tau_{RB}^{prop}(t_1))$ with eqn (4) and (6), similar delay expression is defined as

$$\tau_{AB}^{obs*}(t_1) \stackrel{def}{=} \tau_{RB}^{obs}(t_1) - \tau_{RA}^{obs}(t_1) - \frac{d}{dt}\tau_{AB}^{prop} \cdot \tau_{RA} \quad (8)$$

$$= \tau_{AB}^{prop}(t_1) + \tau_B^{stn} - \tau_A^{stn} + \tau_{RB}^{str} - \tau_{RA}^{str}. \quad (9)$$

Eqn (8) is definition of virtual delay observable τ_{AB}^{obs*} . Difference of virtual observable and true observable of AB baseline is derived by comparing eqn(7) and (9) as

$$\tau_{AB}^{obs*} - \tau_{AB}^{obs} = \tau_{RB}^{str} - \tau_{RA}^{str} - \tau_{AB}^{str}. \quad (10)$$

Then only radio source structure effect is difference from expected true VLBI delay of AB baseline.

3. The NHS VLBI Observation Scheme.

The NHS VLBI observation with small diameter antenna has four major advantages: (1) lower cost, (2) fast slew rate, (3) smaller distortion, and (4) elimination of local effect of large diameter antenna. Point (1) – (3) are obvious due to the properties of small antenna size. The point (4) is confirmed from eqn (9), were station dependent effect of antenna R is eliminated. Point (2) – (4) are important aspect for improving accuracy of geodesy. It is reported that gravitational deformation effect is significant and inevitable for large diameter antenna [13, 14]. Thus, NHS VLBI scheme has a potential to improve geodetic VLBI.

This NHS VLBI did not has reality for practical used before broadband VLBI became available, because delay precision with small diameter antenna has been limited by poor SNR due to small collecting area in legacy S/X observation. However, owing to its large effective bandwidth, broadband VLBI can achieve better than pico second delay precision with minimum SNR of fringe detection. Fig. 3 shows histogram of post-fit residual distribution as an example of NHS VLBI observation data. It demonstrates that post-fit residual distribution of AB baseline does not expand w.r.t. those of original OA, and OB. Weighted root mean square (WRMS) of post-fit residual of AB baseline was even smaller than that of OA, and OB baselines. It indicates that some station dependent contribution from large diameter antenna ‘O’ was commonly removed, then NHS scheme improved the observation precision.

Since NHS VLBI scheme suppose that two nodes and hub have to observe common radio source simultaneously, this is one of the limiting factor of the baseline length. Another draw back is delay error caused by radio source structure effect in group delay represented by eqn (10). Although the NHS VLBI cannot be used earth diameter scale VLBI, it is valuable to investigate its potential to improve the geodetic precision. Radio source structure is subject to be solve in global VGOS observation, then this issue have to be investigated.

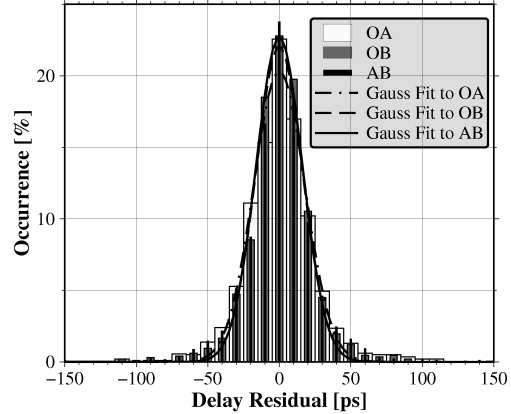


Figure 3. Histogram of post-fit delay residual of OA, OB, and AB baselines in the session of 10-11 July 2016, where delay of AB baseline was computed by the algorithm described in the text (O:Kashima34, A: 1.6m diameter antenna at Tsukuba, and B:2.4m diameter antenna at Koganei). The WRMS of the residuals were 24.5 ps, 23.3 ps, and 22.2 ps for OA, OB, and AB baseline, respectively.

Table 1. Observation parameters in the comparison experiment between NHS and legacy VLBI observation.

| VLBI scheme | NHS Broadband | Legacy S/X |
|-----------------------|---------------|------------|
| Bandwidth per channel | 1024 MHz | 8MHz |
| Number of Channels | 4 | 16 |
| Effective Bandwidth | 1.8 ~ 3.8 GHz | 133MHz |
| Integration time | 1 sec. | 9 sec. |
| SNR | about 10 | about 100 |
| RMS of delay residual | 4 ~ 7 psec | 35 psec |

4. Comparison of Delay Precision between Broadband NHS and Legacy VLBI

An experiment was conducted to compare the delay precision between legacy S/X mode and broadband NHS VLBI. Legacy mode observation was made with 11m diameter antenna pair by using frequency sequence of IVS-T2 session. Broadband NHS VLBI observation data used in this comparison was taken from the series of VLBI experiments in 2016 conducted among 1.6 m antenna installed at National Metrology Institute of Japan (NMIJ), 2.4m antenna at NICT (Koganei), and 34m antenna at Kashima. In both cases, strong radio source were observed for a certain length of time. Then precision of delay observable is evaluated by scattering of data around the mean of detrended delay time series. Alan standard deviations were computed as an indicator of the precision (Fig. 4). Observation parameters are listed in Table 1. This

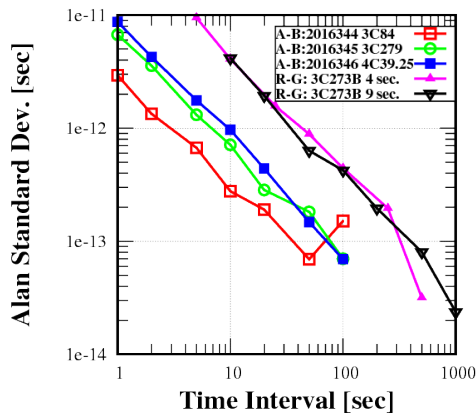


Figure 4. Comparison of delay precision was made by Alan standard deviation between NHS VLBI with antenna group of 2.4m-34m-1.6m and legacy S/X VLBI with 11m antenna pair. Alan standard deviations were computed from detrended time series VLBI delay obtained by continuous tracking of strong radio source.

experiment result indicates an evidence that delay precision of NHS scheme with 1.6m and 2.4m antenna shows higher delay precision than legacy S/X VLBI observation with 11m diameter antenna pair.

5. Summary

The node - hub style (NHS) VLBI with closure delay relation was introduced as a new VLBI observation scheme. Due to large effective bandwidth, broadband NHS has got a reality to be used in geodetic observation. Advantages of the NHS scheme are (1) lower cost, (2) fast slew rate, (3) smaller distortion, and (4) eliminating the local effect of large diameter antenna. To be considered in the NHS scheme is radio source structure effect, which remains in the closure delay relation. Since local effect of large diameter antenna is eliminated in the NHS VLBI, it has a potential to improve the precision of geodetic VLBI.

References

- [1] Sekido, M., et al., "Development Status of GALA-V Broadband VLBI - Geodetic Solution and Clock Comparison -", IVS NICT-TDC News (ISSN 1882-3432), No. 36., pp.20-22, 2016.
- [2] Petrachenko, B. , et al., "Design Aspects of the VLBI2010 System", NASA Technical Memorandum, NASA/TM-2009-214180, ftp://ivscc.gsfc.nasa.gov/pub/misc/V2C/PR-V2C_090417.pdf, 2009.
- [3] Ujihara, H., "Development of wideband feed for Kashima 34m antenna", Radio Sci., Vol.52, pp 476-489, DOI: 10.1002/2016RS006071, 2017.
- [4] Ujihara, H., "Development of Wideband Antenna", IVS NICT-TDC News (ISSN 1882-3432), No. 36., pp.13, 2016.
- [5] Takefuji, K., "Performance of Direct Sampler K6/GALAS", IVS NICT-TDC News(ISSN 1882-3432) No.36, pp.20-22, 2016.
- [6] Kondo, T., & K. Takefuji, "An algorithm of wideband bandwidth synthesis for geodetic VLBI", Radio Sci., 51, doi:10.1002/2016RS006070, 2016.
- [7] Niell, A. E., et al., "Geodetic Measurements with a Mobile VLBI System, Radio Interferometry Techniques for Geodesy", Proceedings of a conference held June 19-21, 1979 at the M. I. T., NASA CP-2115, 3. 1980
- [8] Kaneko, A., et al., "II.5 The 11m Antenna System for Minami-Daito Isl.Station and the Highly Transportable VLBI Station", J. Communications Research Lab., 36 (8), pp65-74, 1990.
- [9] Takashima, K., & M. Ishihara, "The History and Transition of Very long Baseline Survey at Geographical Survey Institute", J. Geod. Soc. Japan., 54(4),205-219,2008.
- [10] Hase, H., et al., "The TIGO-Project", New Technologies in VLBI ASP Conf. Ser., 306, 347-360,2003.
- [11] Gordon, D., & MacMillan, D., "Calc/Solve Software", https://lupus.gsfc.nasa.gov/software_calc_solve.htm
- [12] Charlot, P., "Radio-Source Structure in Astrometric and Geodetic Very Long baseline Interferometry", Astrn. J., 99(4), pp. 1309-1326, 1990.
- [13] Pierguido, S., et al., "Height bias and scale effect induced by antenna gravitational deformations in geodetic VLBI data analysis", J. Geod., 85,pp-18, doi:10.1007/s00190-010-0410-6, 2011.
- [14] Artz, T., Springer, A., and Norhnagel, A., "A complete VLBI delay model for deforming radio telescopes: the Effelsberg case", J. Geod., 88, pp.1145-1161, doi:10.1007/s00190-014-0749-1, 2014.

Holographic Measurement for Kashima 34 meter Antenna

Kazuhiro Takefuji¹ (takefuji@nict.go.jp),
Masanori Tsutsumi¹, Eiji Kawai¹, and
Mamoru Sekido¹

¹ *Kashima Space Technology Center, National Institute of Information and Communications Technology, 893-1 Hirai, Kashima, Ibaraki 314-8501, Japan*

Abstract: We carried out the first VLBI style holographic observation for Kashima 34 meter radio telescope at 12.25 GHz. To operate the holographic observation, we made the reference antenna called MARBLE0 and front/back end system capable to receive 10 - 13 GHz frequency range. Broadband receiver system developed for the GALA-V was used to receive signal of broadcast satellite at 34m antenna. After performing software correlation of the recorded data from MARBLE0 and Kashima 34m, and two-dimensional Fourier transform of it, then we successfully obtained the illumination pattern and surface height distribution. The result will be used for the turning the surface of the 34 meter telescope in near future.

1. Introduction

Since the location of Kashima is close to the Pacific Ocean and the salty wind from the sea blows toward our station, then our antenna is suffered from corrosion. We are planning to make repair work on the back-up structure of Kashima 34 meter parabolic dish from the end of this fiscal year to next year. Some of the antenna panel might have to be removed and restored in the repair work. Thus, surface height measurement and adjustment is required in that case. Then we planned surface height adjustment not only for removing panels in the repair work, but also for whole antenna aperture area to improve antenna efficiency. For the preparation of this project, we have made a holographic surface height measurement of Kashima 34 meter antenna in prior to the repair work in 2018.

2. MARBLE0 as Reference antenna

In the spring of 2017, 1.6-meter diameter main reflector of the compact antennas (MARBLE1) were replaced to 2.4-meter one to improve the sensitivity. We reused the old 1.6-meter dish for the reference antenna of the holographic measurement. Fig 1 and Fig. 2 show the photo of the reference antenna and block diagram of the observing system, respectively. The MARBLE0 reference antenna



Figure 1. Photo of the reference antenna, which we called MARBLE0, and Kashima 34 m antenna behind the MARBLE0 directing toward a satellite.

is composed of 1.6m dish, Misumi aluminum frame pillar parts, and receiver system. This reference station can be easily raised up and fixed manually. Inside the RF box at the focus of the reference antenna, an ambient temperature LNA and amplifier, which works in a frequency range from 10 to 12 GHz, have been installed to receive satellite signals. As for receiving system of Kashima 34m antenna, broadband observation system of GALA-V, which composed of NINJA feed and room temperature LNA, was used to receive signal of broadcasting satellite. Appropriate attenuation was inserted in the receiver system to avoid saturation.

3. Observations

Fig. 3 shows the signal received from the broadcast satellite, JCSAT-3A. Each rectangular shaped spectrum corresponds to modulated digital signal of different channels. The lowest band of 8 MHz width was converted by analog frequency converter and sampled by K5/VSSP32 with 8 bit quantization at 16 MHz sampling rate. High dynamic range is important for accurate holographic measurement. Observation procedure was as follows. Reference station MARBLE0 continuously observe the satellite signal with fixed azimuthal and elevation angle. Kashima 34-meter antenna is operated by a snap schedule file of the Field system 9 (FS9). The snap schedule controls the antenna to obtain complex beam pattern in a rectangular area ($\Delta Az \times \Delta El$) in the sky around the satellite. The antenna sweeps for a certain azimuthal angle (ΔAz) width fixed elevation in one step. Then antenna sweeps back to the same azimuthal angle in opposite direction with elevation angle differs by

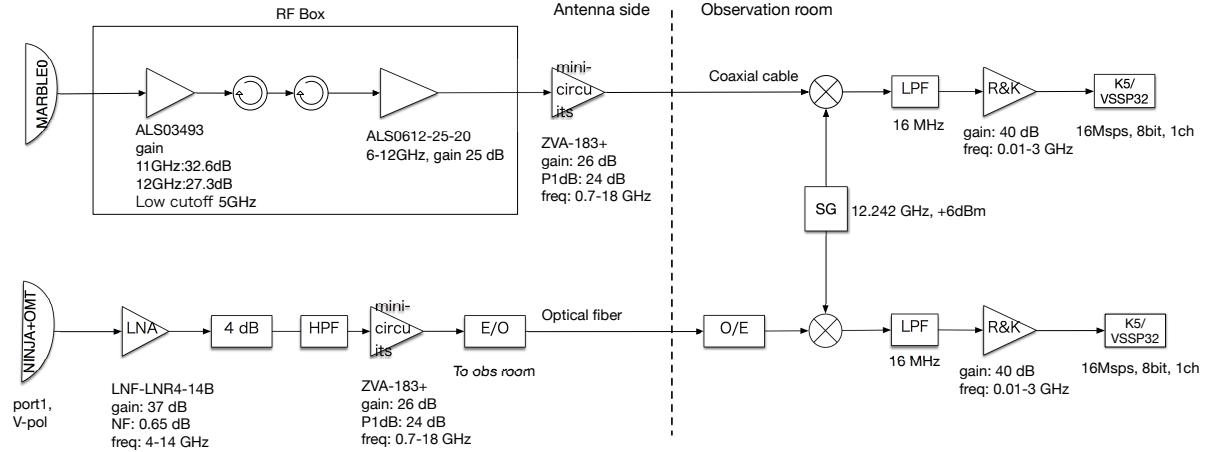


Figure 2. Observing system block diagram of the reference antenna MARBLE0 and broadband Gala-V for the holographic observation.

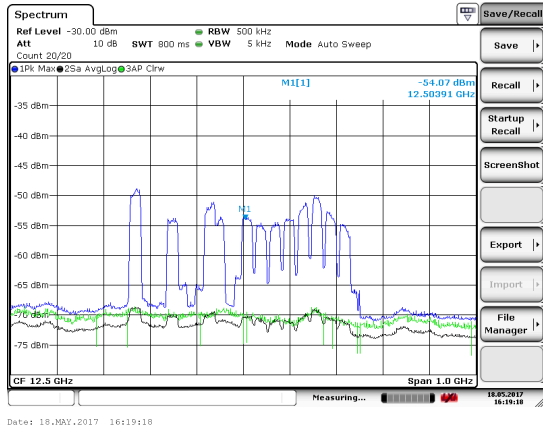


Figure 3. Example of received satellite signal at 12 GHz with the MARBLE0 system

δEl . By repeating this so called 'zigzag scan', beam pattern data is corrected in rectangular sky area. The sweeping ranges ΔAz and ΔEl are set to be 1.4 degrees so that number of points ($\Delta El/\delta El$) becomes 34 with expecting 1 meter spatial resolution. Sweeping in azimuthal direction is made by slow speed slew mode without commanding azimuthal angle position. Actual Az/El angle position data is readout from antenna control unit (ACU) by every second and recorded in log file of FS9. One session of this observation takes about 1.5 hour. After the observation, complex beam pattern is derived by correlation processing with software correlator GICO3. The data processing procedure is,

1. Performing software correlation of 8-bits data by GICO3
2. Searching fringe between 34 m and Marble0 in every 10ms

3. Extracting proper antenna position (0.05 deg step as usual) from log file and matching it with correlation results
4. Performing two dimensional Fourier transform with obtained correlation amplitude and phase with adjusting the peak position.
5. Removing phase slope and offset by least square estimation, and obtaining residual phase, which corresponds to twice of the antenna surface height.

4. Results

Fig. 4 show the correlation amplitude and phase in the azimuth and elevation after the zigzag schedule. Different number of quantization bit was examined before the observation. By acquiring data with changing quantization bit 1, 2, 4, and 8-bits, correlation amplitude of 20, 26, 78.5, and 79.9 were obtained, respectively. By comparing amplitude of signal between power measurement and correlation processing of the data, 8-bit quantization has been selected.

Fig. 5 show the two dimensional amplitude (illumination pattern) and phase (surface height distribution) obtained by two dimensional Fourier transform of the complex beam pattern. We have performed several sessions of this holographic observation for several reasons, such as to determine the correspondence between antenna surface position and obtained surface map, to evaluate the measurement precision, and to confirm the height adjustment direction. Fig. 5 shows the illumination pattern in case that we put a black body absorber on the surface. That absorber corresponds to the slightly dark point seen at the position of (5m, -8m) in horizontal vertical coordinates. Consequently, it

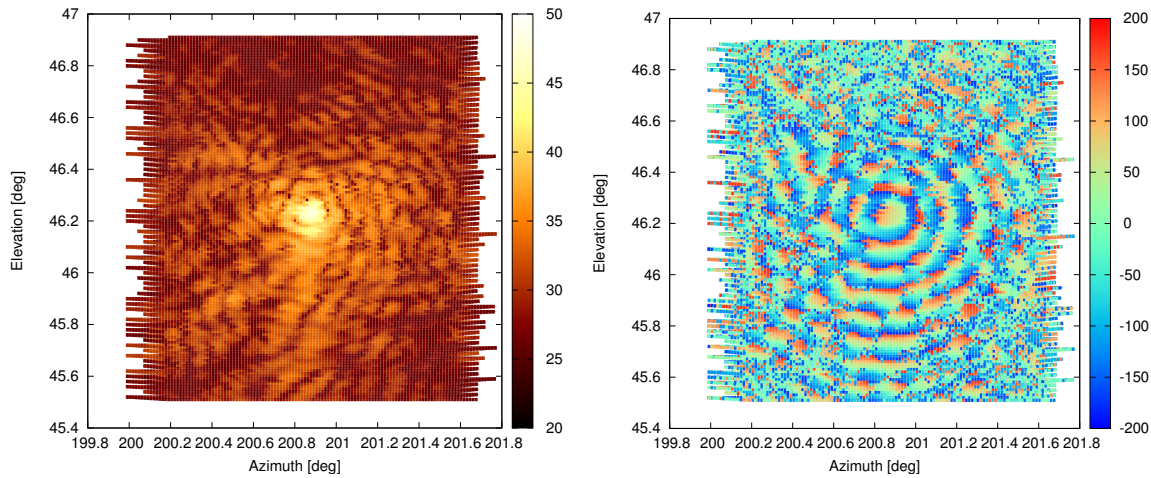


Figure 4. Correlation amplitude(left) and phase (right) after the zigzag schedule

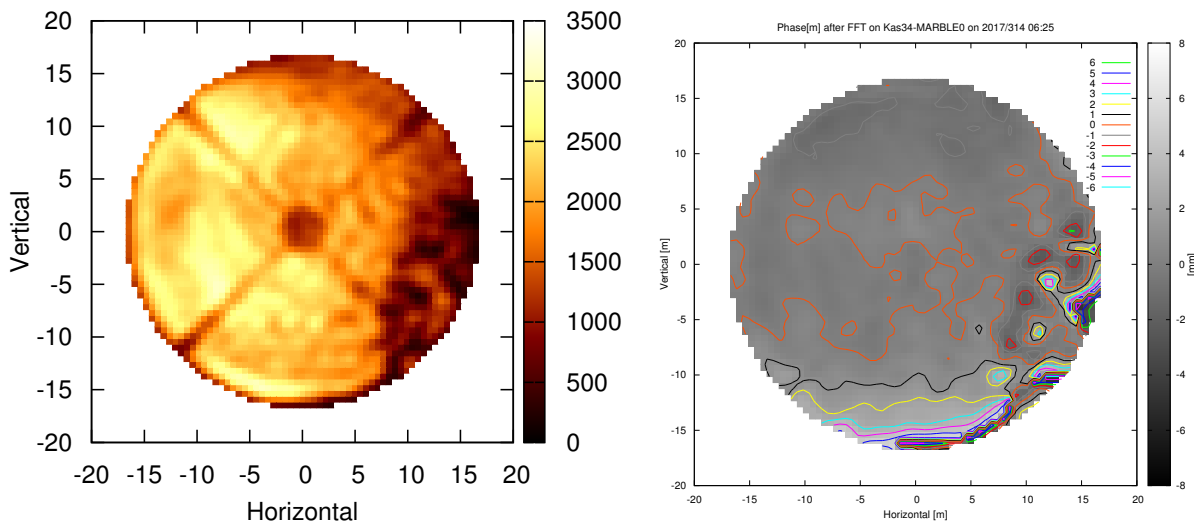


Figure 5. Obtained illumination pattern (left) and surface height distribution (right) of the Kashima 34 meter telescope

was found out that surface is bumpy at the bottom and left side of surface. These height distribution is result of accumulated deformation for 29 years, since no measurement and adjustment have been performed after the construction. This is the first holographic height measurement result for the Kashima 34 meter antenna.

5. Summary

We have carried out the first holographic surface height measurement for Kashima 34 meter radio telescope. To operate the holographic observation, we prepared a reference antenna named MARBLE0 and front/back end system. After software correlation of observed data at MARBLE0 and Kashima 34m, and two-dimensional Fourier transform, we have successfully obtained the illumination pattern

and surface height distribution. This technique will used for the turning the surface of the 34 meter telescope in 2018.

Acknowledgement

We thank Jun Amagai of NICT Okinawa, Hiroshi Mikoshiba, and Kazuyuki Handa of NAO for their kind advices of holographic technique.

Recent progress of K5 software correlation system

Tetsuro Kondo^{1,2}

(kondo@shao.ac.jp, kondo@nict.go.jp)

¹Kashima Space Technology Center
Communications Research Laboratory
893-1 Hirai, Kashima, Ibaraki 314-0012, Japan

²Shanghai Astronomical Observatory
Chinese Academy of Science
80 Nandan Road, Shanghai 200030, China

Abstract: K5 software correlation system consisting of software correlator and fringe search software including a bandwidth synthesis processing has been developed to carry out correlation processing for K5/VSSP series data. Now K5 software correlator can process data with Mark5B and VDIF data formats directly besides the K5 format data. A wideband bandwidth synthesis function is newly implemented in the K5 bandwidth synthesis software named KOMB.

1. Introduction

National Institute of Information and Communications Technology (NICT) has developed the K5 software package dedicated to data obtained by K5/VSSP series sampler (Kondo *et al.*, 2002; Kondo *et al.*, 2004). The software package consists of three categories of processing, that is, 1) “observation”, 2) “correlation processing”, and 3) “fringe search and bandwidth synthesis” as shown in Fig. 1. K5 software correlator is a member of K5 software package that has been developed to carry out correlation processing. Early K5 software correlator could only process K5 format data. Therefore data format conversion software was developed to process other format data, such as Mark-5B and VDIF data formats directly besides the K5 format data. However, it can now handle Mark-5B and VDIF data formats directly besides the K5 format data. Furthermore, conventional bandwidth synthesis software KOMB has been improved to make possible to realize a wideband bandwidth synthesis with a bandwidth of 10 GHz or more by using an algorithm developed by Kondo and Takefuji (2016). These new functions are introduced in this report.

2. Revised software correlator

K5 software correlator has been revised to handle Mark-5B and VDIF format data directly. Correlation processing between different data formats is also supported. Fig. 2 shows an example of results of correlation processing between

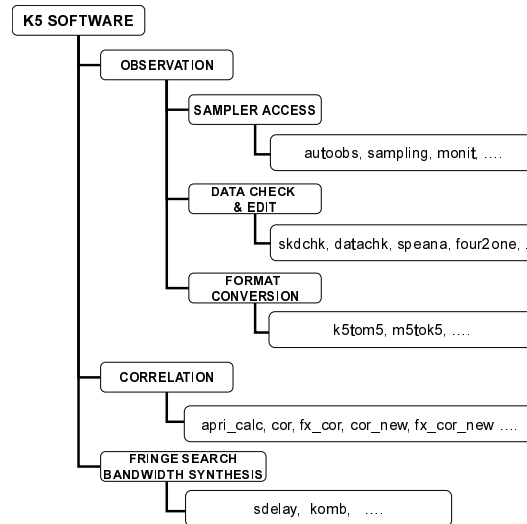


Figure 1. Contents of K5 software package.

K5/VSSP data (KASHIM11) and Mark-5B format data (TOMAKO11). Coarse fringe search results are presented for 4 channels among 16 channels. As for TOMAKO11, K5/VSSP data are converted to Mark-5B format data for checking software correlator.

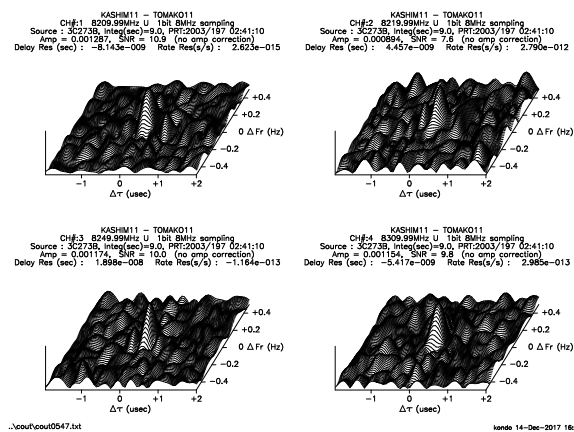


Figure 2. An example of correlation results between K5/VSSP format (KASHIM11) and Mark-5B format (TOMAKO11) data.

3. Wideband bandwidth synthesis

Correlated data are processed by the K5 bandwidth synthesis software KOMB (Kondo *et al.*, 1999) to get precise residual delay by synthesizing multi-channel correlated data. Now KOMB can make a bandwidth synthesis with a bandwidth of 10 GHz or more. Figs. 3 and 4 shows a flowchart of wideband bandwidth synthesis (WBWS) without

the use of phase calibration signals. At first, a reference scan is selected to determine phase and delay calibration data for a WBWS processing. Then each scan is processed. Differential total electron content (TEC) is also estimated in the WBWS processing (see Kondo and Takefuji (2016) for details).

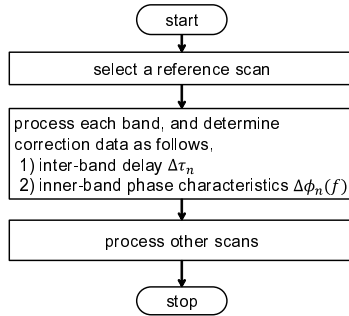


Figure 3. A flowchart of wideband bandwidth synthesis (WBWS) without phase calibration signals.

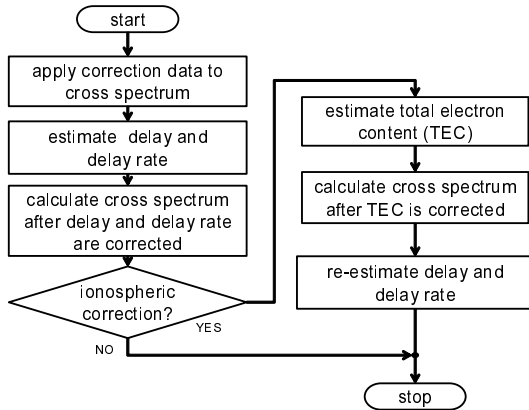


Figure 4. A flowchart of the processing of each scan.

Fig. 5 shows an example of WBWS results without phase and delay corrections. Left panel shows a cross spectrum and right panel a search function. Lower panel in the cross spectrum shows a residual phase. As shown in the figure, residual phases are rotating with respect to the frequency. This means that WBWS failed. Peak position denotes residual delay and delay rate in the plot of search function, but in this case, the peak is spread in the direction of delay. However after phase and delay correction, residual phases are aligned in the frequency direction and the peak in the search function becomes clear as shown in Fig. 6.

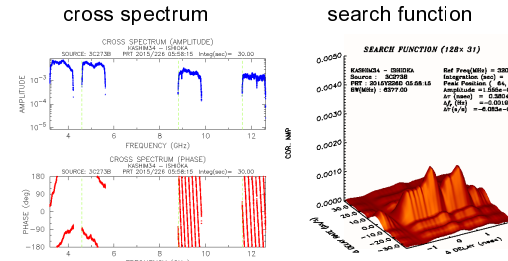


Figure 5. An example of wideband bandwidth synthesis without phase and delay corrections (left panel: cross spectrum, right panel: search function). Phases are not aligned and peak in search function is spread in the delay direction.

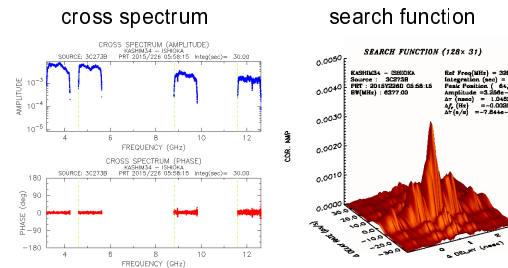


Figure 6. An example of wideband bandwidth synthesis with phase and delay corrections.

References

Kondo, T., M. Sekido, and H. Kiuchi, KSP bandwidth synthesizing software, J. Commun. Res. Lab., 46, 67-76, 1999.

Kondo, T., Y. Koyama, J. Nakajima, M. Sekido, R. Ichikawa, E. Kawai, H. Okubo, H. Osaki, M. Kimura, Y. Ichikawa, and GALAXY team, Real-time Gigabit VLBI system and Internet VLBI system, IVS 2002 General Meeting Proceedings, pp.142-146, 2002.

Kondo, T., M. Kimura, Y. Koyama, and H. Osaki, Current status of software correlators developed at Kashima Space Research Center, IVS 2004 General Meeting Proceedings, edited by N. R. Vandenberg and K. D. Baver, NASA/CP-2004-212255, pp.186-190, 2004.

Kondo, T., and K. Takefuji, An algorithm of wideband bandwidth synthesis for geodetic VLBI, Radio Sci., Vol. 51, doi:10.1002/2016RS006070, 2016.

“IVS NICT Technology Development Center News” (IVS NICT-TDC News) published by the National Institute of Information and Communications Technology (NICT) (former the Communications Research Laboratory (CRL)) is the continuation of “IVS CRL Technology Development Center News” (IVS CRL-TDC News). (On April 1, 2004, Communications Research Laboratory (CRL) and Telecommunications Advancement Organization of JAPAN (TAO) were reorganized as “National Institute of Information and Communications Technology (NICT)”.)

VLBI Technology Development Center (TDC) at NICT is supposed

- 1) to develop new observation techniques and new systems for advanced Earth's rotation observations by VLBI and other space techniques,
- 2) to promote research in Earth rotation using VLBI,
- 3) to distribute new VLBI technology,
- 4) to contribute the standardization of VLBI interface, and
- 5) to deploy the real-time VLBI technique.

The NICT TDC newsletter (IVS NICT-TDC News) is published biannually by NICT.

This news was edited by Mamoru SEKIDO, Kashima Space Technology Center. Inquires on this issue should be addressed to Mamoru SEKIDO, Kashima Space Technology Center, National Institute of Information and Communications Technology, 893-1 Hirai, Kashima, Ibaraki 314-8501, Japan, e-mail : sekido@nict.go.jp.

Summaries of VLBI and related activities at the National Institute of Information and Communications Technology are on the Web. The URL to view the home page of the Radio Astronomy Applications Section of the Space-Time Measurement Group of Space-Time Standards Laboratory is : “<http://www2.nict.go.jp/sts/stmg/ivstdc/news-index.html>”.

IVS NICT TECHNOLOGY DEVELOPMENT CENTER NEWS No.37, December 2017

International VLBI Service for Geodesy and Astrometry
NICT Technology Development Center News
published by

National Institute of Information and Communications Technology, 4-2-1 Nukui-kita, Koganei,
Tokyo 184-8795, Japan

